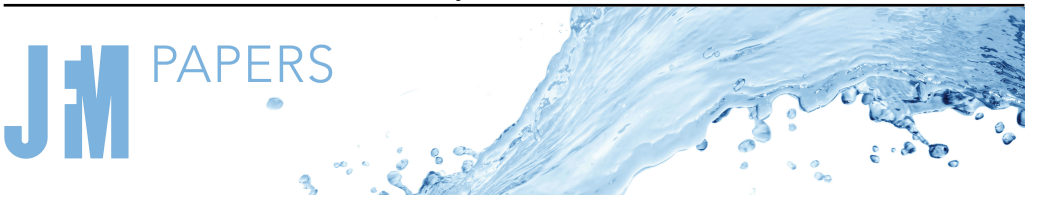
J. Fluid Mech. (2026), *vol.* 1039, A9, doi:10.1017/jfm.2026.11808



A radiation two-phase flow model for simulating plasma–liquid interactions

Ke-Jian Qian[1,†], **Zhu-Jun Li**[1,†], **Tao Tao**[2,*], **De-Hua Zhang**[1], **Rui Yan**[1,*] **and Hang Ding**[1]

[1]State Key Laboratory of High Temperature Gas Dynamics, School of Engineering Science, University of Science and Technology of China, Hefei 230026, PR China

[2]Department of Plasma Physics and Fusion Engineering, University of Science and Technology of China, Hefei 230026, PR China

Corresponding authors: Rui Yan, ruiyan@ustc.edu.cn; Hang Ding, hding@ustc.edu.cn

(Received 12 January 2026 UTC; revised 7 June 2026 UTC; accepted 14 June 2026 UTC)

In laser-produced plasma (LPP) extreme ultraviolet (EUV) sources, deformation of a tin droplet into an optimal target shape is determined by its interaction with a pre-pulse laser-generated plasma. This interaction is mediated by a transient ablation pressure, whose complex spatio-temporal evolution remains experimentally inaccessible. Existing modelling approaches are limited: empirical pressure–impulse models neglect dynamic plasma feedback, while advanced radiation hydrodynamics codes often fail to resolve late-time droplet hydrodynamics. To bridge this gap, we propose a radiation two-phase flow model based on a diffuse interface approach. The model integrates radiation hydrodynamics for the plasma with the Euler equations for a weakly compressible liquid, extending a five-equation diffuse interface formulation to incorporate radiation transport, thermal conduction, ionisation and surface tension. This formulation enforces pressure and velocity equilibrium across the diffuse interface region, with closure models constructed to ensure correct jump conditions at interfaces and asymptotically recover the pure-phase equations in bulk regions. Then we apply the model to simulate a benchmark pre-pulse scenario, where a 50 μm tin droplet is irradiated by a 10 ns laser pulse. Our axisymmetric simulations capture the rapid plasma expansion and subsequent inertial flattening of the droplet into a thin, curved sheet over microsecond time scales. Notably, the model reproduces experimentally observed features such as an axial jet – rarely replicated in prior simulations. Quantitative agreement with experimental data for sheet dimensions and velocity validates the approach. The proposed model self-consistently

* Joint Team for the Double-cone Ignition Scheme.

†The authors contributed equally to the article.

© The Author(s), 2026. Published by Cambridge University Press.

https://doi.org/10.1017/jfm.2026.11808 Published online by Cambridge University Press

couples laser–plasma physics with compressible droplet dynamics, providing a powerful tool for studying plasma–liquid interactions in LPP-EUV source optimisation.

Key words: plasmas, drops, multiphase flow

1. Introduction

Laser-produced plasmas (LPPs) are the sources of extreme ultraviolet (EUV) light for nanolithography (Versolato 2019). Generation of EUV light in a modern LPP-EUV device involves two steps: a relatively low intensity pre-pulse laser is to prepare the target by deforming a tin droplet into a proper tin sheet; then a subsequent main pulse heats it up to produce EUV-emitting plasmas (Mizoguchi *et al.* 2010; van de Kerkhof *et al.* 2020). To maximise the conversion efficiency and minimise tin debris, a precise control of droplet shape induced by the pre-pulse is crucial (Versolato *et al.* 2022) and requires in-depth understanding on the droplet–plasma dynamics (Meijer *et al.* 2022). Upon pre-pulse impact, asymmetric plasma expansion from localised laser energy absorption exerts very high pressure at the droplet's illuminated surface (Basko, Novikov & Grushin 2015; Kurilovich *et al.* 2018; Sheil *et al.* 2024). This pressure, usually referred to as the ablation pressure, not only launches acoustic waves travelling inside the droplet (Reijers, Snoeijer & Gelderblom 2017), but also propels the droplet and simultaneously deforms it into a thin sheet that eventually fragments (Gelderblom *et al.* 2016). The ablation pressure represents the interaction between the plasma and the droplet, and its spatial distribution significantly changes with time. However, the ablation pressure profile remains experimentally unmeasurable.

To numerically investigate droplet dynamics, different ablation pressure models have been proposed to mimic the impact from the plasma (Klein *et al.* 2015; Gelderblom *et al.* 2016; França *et al.* 2025). In the numerical simulations, the droplet was assumed to be incompressible and inviscid. Gelderblom *et al.* (2016) simulated deformation of a droplet after being impacted by a laser pulse using a boundary integral method coupled with a simplified ablation pressure model. Different ablation pressure profiles, including Gaussian-shaped, cosine-shaped and focused-on-point, were found to drive the droplet into different shapes. To determine the dependence of droplet deformation on the pressure pulse duration at constant total momentum, an analytical acoustic model (assuming small density fluctuations) was further derived for the internal pressure, pressure impulse and velocity fields (Reijers *et al.* 2017). However, it was reported that tin sheets produced in experiments and most advanced EUV light sources often curve in a direction opposite to the theoretical predictions (Kurilovich *et al.* 2016; Hernandez-Rueda *et al.* 2022; França *et al.* 2025). An instantaneous pressure impulse described by a raised cosine function was introduced to be able to reproduce the curvature inversion in the simulations (França *et al.* 2025). Droplet fragmentation was investigated via two-fluid simulations also in the framework of applying a pressure impulse on an incompressible droplet (Nykteri & Gavaises 2022). The results showed a good agreement with the experimental observations of Klein *et al.* (2015) with respect to the expansion of the liquid sheet and the development of a polydisperse cloud of fragments. Although the pressure–impulse modellings are convenient to be employed in simulations on the droplet dynamics, the pressure–impulse profiles (spatial and temporal) need to be empirically prescribed. Moreover, it is challenging to consider the dynamic feedback of the droplet to the plasma, which is expected to adjust the pressure profiles in flight.

https://doi.org/10.1017/jfm.2026.11808 Published online by Cambridge University Press

On the other hand, droplet dynamics can be obtained from direct numerical simulations that comprehensively take all the important physical processes into account. Radiation hydrodynamics (RHD) codes, such as FLASH (Fryxell *et al.* 2000), HEIGHTS (Sizyuk & Hassanein 2015), HELIOS-CR (MacFarlane, Golovkin & Woodruff 2006), RALEF (Basko *et al.* 2012) and RHDLPP (Min *et al.* 2024), consider detailed modellings on the key LPP-relevant processes, including laser absorption, radiation transport and heat conduction, and they have been used for LPP-EUV simulations (Sheil *et al.* 2023). Kurilovich *et al.* (2018) performed simulations of interactions between a nanosecond pre-pulse and a tin droplet using two-dimensional (2-D) RALEF code, and obtained a power-law scaling of propulsion velocity versus laser energy that agrees well with experimental data. The ratio of propulsion speed and initial radial expansion rate on a broad range of parameters (including laser energies, spot sizes and droplet sizes) given by the RALEF simulations (Hernandez-Rueda *et al.* 2022) were shown to agree well with the experiments, and the energy partitioning between the deformation and the propulsion of the droplet was consistent with the instantaneous pressure-driven droplet simulations by Gelderblom *et al.* (2016). Nevertheless, the RHD modellings were based on a single-fluid framework and required a unified equation of state (EOS) like the Frankfurt EOS (Faik *et al.* 2012) to model tin coexisting in various states during the pre-pulse stage. While the RHD codes have been shown to be effective for simulating the laser–plasma interactions and the early phase of the droplet deformation, it was recently reported that an RHD code could not adequately simulate late-time droplet deformation (França *et al.* 2025). This shortcoming likely explains why investigations into the later droplet dynamics such as thin-sheet formation and fragmentation (Klein *et al.* 2020; Liu *et al.* 2022) still largely rely on pure hydrodynamics simulations (Liu *et al.* 2017). Therefore, the development of a radiation two-phase flow model, capable of simulating plasma physics, long-term evolution of droplet and their interactions, is a critical objective for LPP-EUV research.

In this paper, we propose a radiation two-phase flow model for the plasma–liquid interactions, based on a diffuse interface methodology. Specifically, we integrate RHD for the plasma with the Euler equations for a compressible liquid, by extending a five-equation diffuse interface formulation (Kapila *et al.* 2001; Allaire, Clerc & Kokh 2002) to incorporate key physics: radiation transport, thermal conduction, ionisation and surface tension. In particular, the model enforces pressure and velocity equilibrium across the diffuse interface region, incorporates surface tension as a volumetric force in the momentum equation, and is capable of handling two different fluids with large density contrasts. To ensure physical fidelity, we develop closure models for energy fluxes and sources within the interface region. These closures guarantee the correct jump conditions at interfaces, and ensure that the model asymptotically recovers the pure-phase governing equations in bulk regions. We validate the model by demonstrating its accurate treatment of radiation transport and thermal conduction, and confirm that it correctly reduces to compressible two-phase flows in the absence of radiative effects. Finally, to evaluate its capability for self-consistently coupling laser–plasma physics with compressible droplet dynamics, we apply the radiation two-phase flow model to simulate a benchmark pre-pulse scenario, where a 50 μm tin droplet is irradiated by a 10 ns laser pulse.

The rest of this paper is organised as follows. Section 2 introduces the governing equations and EOS for the bulk fluids. In § 3, a new diffuse interface model is derived by unifying the governing equations for the liquid and plasma phases, and appropriate mixture closure relations are proposed. Section 4 presents a suitable numerical scheme for solving the model. Section 5 provides validation through several test cases: simulations of radiation–plasma flows and liquid–gas two-phase flows are compared against established results from the literature. In § 6, the model is applied to simulate the deformation of a tin

https://doi.org/10.1017/jfm.2026.11808 Published online by Cambridge University Press

droplet irradiated by a nanosecond laser pulse. Finally, § 7 summarises the conclusions of this work.

2. Governing equations and EOS for bulk fluids

In this section, we present the governing equations and EOS for the plasma and the liquid considered. In particular, we use the RHD model for the plasma and the Euler equations for the liquid.

2.1. *The RHD for the plasma*

A plasma in the presence of radiation photons can be modelled with a set of RHD equations (Castor 2004) in the form

$$\begin{cases} \partial_t \rho_g + \nabla \cdot (\rho_g \boldsymbol{u}_g) = 0, \\ \partial_t (\rho_g \boldsymbol{u}_g) + \nabla \cdot (\rho_g \boldsymbol{u}_g \boldsymbol{u}_g) + \nabla (p_g + p_r) = 0, \\ \partial_t (\rho_g e_g) + \nabla \cdot (\rho_g e_g \boldsymbol{u}_g) + p_g \nabla \cdot \boldsymbol{u}_g = \nabla \cdot (\lambda_g \nabla T_g) + \omega_{r,g} \left(T_r^4 - T_g^4\right), \\ \partial_t E_r + \nabla \cdot (E_r \boldsymbol{u}) + p_r \nabla \cdot \boldsymbol{u} = \nabla \cdot \left(\chi_{r,g} \nabla T_r^4\right) + \omega_{r,g} \left(T_g^4 - T_r^4\right), \end{cases} \tag{2.1}$$

where the subscripts g and r denote plasma (i.e. ionised gas) and radiation, respectively, t is the time, and the plasma quantities include the mass density ρ_g, the macroscopic velocity $\boldsymbol{u}_g$, the pressure p_g, the temperature T_g, the specific internal energy e_g, and the thermal conduction coefficient λ_g. The two components of the plasma, i.e. electrons and ions, are assumed to have identical macroscopic fluid velocity and temperature, and act as a single fluid in this model. Radiation has been modelled under a diffusion approximation, which is valid in an optically thick regime (Castor 2004) where the mean free paths of radiative photons are much shorter than the characteristic length scale of hydrodynamics. The radiation photons act as an ideal gas in an optically thick regime (Castor 2004), and provide a radiation pressure p_r. They are assumed to follow the Planckian (black-body) distribution with radiation temperature T_r that is allowed to differ from the local plasma temperature T_g. The radiation energy $E_r = aT_r^4$ (where $a = 7.5657 \times 10^{-16}$ J m^{-3} K^{-4} is the radiation constant) given by the Planckian distribution is linked with p_r as $p_r = E_r/3$ due to the Eddington approximation (Castor 2004). Once T_r differs from T_g, the radiation photons exchange energy with the plasma at an energy exchange rate $\omega_{r,g}$. Under the diffusion approximation, the energy transported by radiation photons can be effectively separated into two components: one part acts as an energy diffusion process, characterised by the coefficient $\chi_{r,g}$, while the remaining portion contributes to energy convection alongside the plasma flow, as demonstrated in the last equation of (2.1). The simplified radiation model adopted here, which relies on the Planckian distribution approximation, is generally sufficient to capture the essential hydrodynamic behaviour. This approach has been successfully applied in LPP-EUV simulations (Yuan *et al.* 2022), and proves adequate for the pre-pulse simulations performed in our study.

The last two equations in (2.1) are the energy equations for the plasma and the radiation, respectively. Alternatively, the combination of these two equations yields the equation for the total energy of the system:

$$\begin{aligned} \partial_t \left[\rho_g \left(e_g + |\boldsymbol{u}_g|^2/2\right) + E_r\right] + \nabla \cdot \left[\rho_g \left(e_g + |\boldsymbol{u}_g|^2/2\right) \boldsymbol{u}_g + E_r \boldsymbol{u}_g\right] + \nabla \cdot \left[(p_g + p_r) \boldsymbol{u}_g\right] \\ = \nabla \cdot (\lambda_g \nabla T_g) + \nabla \cdot \left(\chi_{r,g} \nabla T_r^4\right). \end{aligned} \tag{2.2}$$

https://doi.org/10.1017/jfm.2026.11808 Published online by Cambridge University Press

Fluid	γ_l	$P_{\infty,l}$ (Pa)	$c_{v,l}$ (J kg^{-1} K^{-1})
Water	4.4	6×10^8	1816
Liquid tin	30	1.421×10^9	210

Table 1. The SG parameters for two liquids considered in the present work.

2.2. *Euler equations for the liquid*

The liquid is assumed to be inviscid and weakly compressible, and its dynamics is governed by the Euler equations

$$\begin{cases} \partial_t \rho_l + \boldsymbol{\nabla} \cdot (\rho_l \boldsymbol{u}_l) = 0, \\ \partial_t (\rho_l \boldsymbol{u}_l) + \boldsymbol{\nabla} \cdot (\rho_l \boldsymbol{u}_l \boldsymbol{u}_l) + \boldsymbol{\nabla} p_l = 0, \\ \partial_t \left[\rho_l \left(e_l + |\boldsymbol{u}_l|^2/2\right)\right] + \boldsymbol{\nabla} \cdot \left[\rho_l \left(e_l + |\boldsymbol{u}_l|^2/2\right)\boldsymbol{u}_l\right] + \boldsymbol{\nabla} \cdot (p_l \boldsymbol{u}_l) = 0, \end{cases} \tag{2.3}$$

where subscript l denotes liquid, and ρ_l, $\boldsymbol{u}_l$, p_l and e_l are density, velocity, pressure and specific internal energy of the liquid, respectively. In order to be consistent with the RHD equations (2.1), the energy equation in (2.3) is reformulated as the transport equation for the internal energy:

$$\partial_t (\rho_l e_l) + \boldsymbol{\nabla} \cdot (\rho_l e_l \boldsymbol{u}_l) + p_l \boldsymbol{\nabla} \cdot \boldsymbol{u}_l = 0. \tag{2.4}$$

The liquid is assumed to be very opaque to radiation, and the self-emission of the liquid is negligibly weak due to its low temperature. Although placed in an radiative environment, the radiation energy of and the radiation transport inside the liquid are neglected, and thus are absent in (2.3). So is heat conduction in the liquid, which is also negligible compared to that in the plasma.

2.3. *The EOS*

The plasma and the liquid have different material properties and thus obey different forms of EOS. We employ the stiffened gas (SG) model (Shyue 1998), which is able to describe the EOS of different materials in a unified form by tuning parameters, for both fluids.

The EOS of the liquid reads

$$\begin{cases} p_l + \gamma_l P_{\infty,l} = (\gamma_l - 1)\rho_l e_l, \\ \rho_l e_l = \rho_l c_{v,l} T_l + P_{\infty,l}, \end{cases} \tag{2.5}$$

where the specific heat ratio γ_l, the reference pressure $P_{\infty,l}$, and the specified heat capacity at constant volume $c_{v,l}$ (Le Métayer *et al.* 2004) are three constant parameters that need to be assigned. The values of γ_l and $P_{\infty,l}$ are usually chosen such that the sound speed inside the liquid,

$$C_l = \sqrt{\gamma_l \left(p_l + P_{\infty,l}\right)/\rho_l}, \tag{2.6}$$

is close to reality (Shyue 1998). Typical choices of γ_l, $P_{\infty,l}$ and $c_{v,l}$ for two liquids in the present work are listed in table 1, to recover a reference state under the standard atmospheric pressure: $T_l = 300$ K, $\rho_l = 1000$ kg m^{-3}, $C_l = 1450$ m s^{-1} for water; $T_l = 593$ K, $\rho_l = 6980$ kg m^{-3}, $C_l = 2471$ m s^{-1} for liquid tin.

https://doi.org/10.1017/jfm.2026.11808 Published online by Cambridge University Press

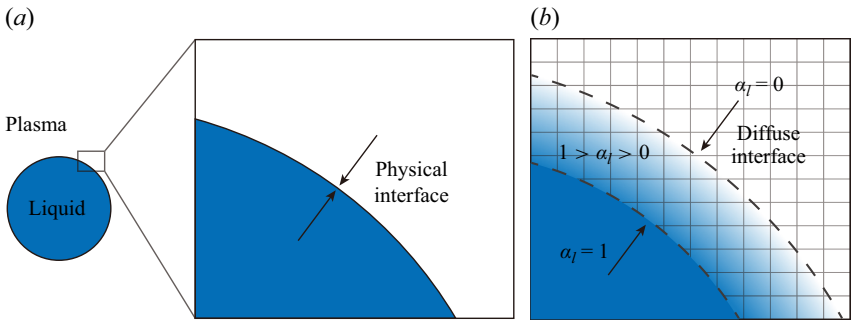


Figure 1. (*a*) Schematic of an interface separating the immiscible plasma and liquid, where the blue phase represents the liquid, and the white phase represents the plasma. (*b*) A diffuse interface is used to replace the physical interface on a Cartesian grid, and the volume fraction of the liquid α_l is adopted to represent the interface position, where $0 \leqslant \alpha_l \leqslant 1$.

A weakly coupled plasma behaves like an ideal gas (Krall & Trivelpiece 1973), corresponding to a particular SG with the reference pressure $P_{\infty,g}$ set to zero. Its EOS reads

$$\begin{cases} p_g = (\gamma_g - 1)\rho_g e_g, \\ \rho_g e_g = \rho_g c_{v,g} T_g, \end{cases} \tag{2.7}$$

where the specific heat ratio γ_g is set to $5/3$. Here, $c_{v,g}$ is the specified capacity at constant volume considering the average ionisation degree (Z_g) as

$$c_{v,g} = \frac{R(1 + Z_g)}{(\gamma_g - 1)M_g}. \tag{2.8}$$

Here, $R = 8.314$ J (mol K)$^{-1}$ is the universal gas constant, and M_g is the molar mass of the element (118.71 g mol^{-1} for tin). The sound speed in the plasma is written in a form similar to (2.6):

$$C_g = \sqrt{\gamma_g p_g / \rho_g}. \tag{2.9}$$

Note that C_g can be an order of magnitude larger than C_l, e.g. a typical tin plasma emitting the interested EUV lights has T_g ranging from 10^5 to 5×10^5 K (Nishihara *et al.* 2008), yielding C_g from 11 000 to 25 000 m s^{-1}.

3. Diffuse interface model

In this section, we establish a diffuse interface model for plasma–liquid interactions, and particularly focus on the exchange of momentum and energy between the plasma and the liquid.

3.1. *Jump conditions at interfaces*

In this work, we model the interface between plasma and liquid as a sharp contact discontinuity with no phase transition or chemical reaction, as illustrated in figure 1(*a*). The two phases are spatially separated and immiscible, with distinctly different material properties, thereby leading to jump conditions at interfaces. Since the interface is essentially a contact discontinuity, the normal velocity and pressure are continuous across the interface in the absence of surface tension, i.e. $\boldsymbol{u}_l \cdot \boldsymbol{n} = \boldsymbol{u}_g \cdot \boldsymbol{n}$ and $p_l = p_g$, where $\boldsymbol{n}$ is the unit normal vector to the interface, while the density is discontinuous, $\rho_l \neq \rho_g$.

https://doi.org/10.1017/jfm.2026.11808 Published online by Cambridge University Press

In contrast, surface tension induces a pressure jump across the interface. Apart from these, the thermal fluxes in the plasma are assumed to vanish at interfaces, due to the comparatively negligible thermal conduction coefficient of the liquid. Similarly, the radiation energy fluxes are also expected to vanish at the interface because of high opacity of the liquid. In the present study, all these conditions are well handled by the proposed diffuse interface model introduced in § 3.2 together with the mixing rules introduced in §§ 3.3 and 3.4.

3.2. *Diffuse interfaces*

In diffuse interface models, the sharp interface between two immiscible fluids is replaced by a diffuse interface with finite thickness where the two fluids are mixed, and the jump conditions at the interface are realised by mixing rules in the diffuse interface region. Inspired by the concept of the diffuse interface, specifically the transport five-equation model (Allaire *et al.* 2002), we propose a diffuse interface model for liquid–plasma interactions, where the volume fraction of the liquid (α_l) is used to represent the interface position, as illustrated in figure 1(*b*). We can see that α_l rapidly changes from 1 on the liquid side to 0 on the plasma side within a thin layer, which is referred hereafter to as the diffuse interface region. In the diffuse interface region, the fluid is treated as a homogeneous mixture of the liquid and the plasma.

Similar to the model of Allaire *et al.* (2002), the proposed model assumes that the velocities and pressures of the two phases are in equilibrium (namely mechanical equilibrium) in the diffuse interface region – i.e. the mixture velocities are $\boldsymbol{u} = \boldsymbol{u}_l = \boldsymbol{u}_g$, and the mixture pressures are $p = p_l = p_g$ – but can be in thermal non-equilibrium ($T_l \neq T_g$). Such mechanical equilibrium at the interface ensures the proper propagation of acoustic waves across material interfaces while allowing the fluids to have different densities, internal energies and EOS. Following the continuous surface force formulation (Garrick, Owkes & Regele 2017), the surface tension is incorporated as a volumetric force in the momentum equation. As a result, we can tentatively write the diffuse interface model for liquid–plasma interactions, which consists of an interface evolution equation, two phasic mass equations, a mixture momentum equation, a mixture energy equation and a radiation energy equation (note that the liquid-phase region is also encompassed by the radiation field, with the radiation energy being set to zero):

$$\begin{cases} \partial_t \alpha_l + \boldsymbol{u} \cdot \nabla \alpha_l = 0, \\ \partial_t (\rho_l \alpha_l) + \nabla \cdot (\rho_l \alpha_l \boldsymbol{u}) = 0, \\ \partial_t (\rho_g \alpha_g) + \nabla \cdot (\rho_g \alpha_g \boldsymbol{u}) = 0, \\ \partial_t (\rho \boldsymbol{u}) + \nabla \cdot (\rho \boldsymbol{u}\boldsymbol{u}) + \nabla (p + p_r) = \sigma \kappa \, \nabla \phi, \\ \partial_t (\rho e) + \nabla \cdot (\rho e \boldsymbol{u}) + p \, \nabla \cdot \boldsymbol{u} = -\nabla \cdot \boldsymbol{q} + S_r, \\ \partial_t E_r + \nabla \cdot (E_r \boldsymbol{u}) + p_r \, \nabla \cdot \boldsymbol{u} = -\nabla \cdot \boldsymbol{F}_r - S_r, \end{cases} \tag{3.1}$$

where ρ and e are the density and the specific internal energy of the mixture, respectively, σ is the surface tension coefficient, $\kappa = -\nabla \cdot (\nabla \phi / |\nabla \phi|)$ is the interface curvature, and ϕ is an order parameter to identify the interface region where the surface tension is applied.

In our diffuse interface model, the absence of an anti-diffusion term implies that the interface thickness (represented by the α contours) may increase over time. To restrict the surface tension force to the vicinity of the droplet interface, we therefore employ ϕ instead

https://doi.org/10.1017/jfm.2026.11808 Published online by Cambridge University Press

of α. The parameter ϕ is defined as

$$\phi = \begin{cases} 1 & \text{if } \alpha_l > 0.9, \\ \min\left[\max\left((\rho - \rho_{min})/(\rho_{max} - \rho_{min}), 0\right), 1\right] & \text{if } 0.1 \leqslant \alpha_l \leqslant 0.9, \\ 0 & \text{if } \alpha_l < 0.1, \end{cases} \tag{3.2}$$

where ρ_{min} and ρ_{max} are set to 1 g cm^{-3} and 4 g cm^{-3}, respectively. As a result, the surface tension force is confined to the interface region bounded by $[\rho_{min}, \rho_{max}]$ and $0.1 \leqslant \alpha_l \leqslant 0.9$.

The energy flux due to thermal conduction $\boldsymbol{q}$, the energy deposition rate to the mixture from radiation S_r, and the energy flux due to radiation diffusion $\boldsymbol{F}_r$, are applied to the mixture; their detailed expressions are provided in § 3.4. It is worth noting that the proposed model of (3.1) reduces to the original transport five-equation model for compressible two-phase flows (Allaire *et al.* 2002) in the absence of thermal conduction and radiation transport (i.e. p_r, E_r, S_r, $\boldsymbol{q}$ and $\boldsymbol{F}_r$ are all zero). Equation (3.1) are not closed yet until the EOS of the mixture is supplied.

3.3. *The EOS in the diffuse interface region*

In the absence of phase transition and chemical reaction, we establish the EOS for the mixture in a similar manner as in Allaire *et al.* (2002). In the diffuse interface region, the conservation of mass and energy straightforwardly leads to ρ and e in the forms

$$\rho = \rho_l \alpha_l + \rho_g \alpha_g, \tag{3.3}$$

$$\rho e = \rho_l \alpha_l e_l + \rho_g \alpha_g e_g, \tag{3.4}$$

respectively. The isobaric closure (Allaire *et al.* 2002) is adopted, namely assuming that the mixture is in mechanical (pressure) equilibrium:

$$p = p_l(\rho_l, e_l) = p_g(\rho_g, e_g). \tag{3.5}$$

Substituting the EOS of the liquid (2.5) and that of the plasma (2.7) into (3.4) under the pressure equilibrium condition of (3.5) readily yields the EOS for the mixture:

$$\left(\frac{\alpha_l}{\gamma_l - 1} + \frac{\alpha_g}{\gamma_g - 1}\right) p = \rho e - \left(\frac{\alpha_l \gamma_l P_{\infty,l}}{\gamma_l - 1} + \frac{\alpha_g \gamma_g P_{\infty,g}}{\gamma_g - 1}\right), \tag{3.6}$$

which can also be expressed in a neater form similar to the SG model as

$$p + \gamma P_\infty = (\gamma - 1)\rho e, \tag{3.7}$$

where the specific heat ratio γ and the reference pressure P_∞ of the mixture are defined as

$$\begin{cases} \dfrac{1}{\gamma - 1} = \dfrac{\alpha_l}{\gamma_l - 1} + \dfrac{\alpha_g}{\gamma_g - 1}, \\ \dfrac{\gamma P_\infty}{\gamma - 1} = \dfrac{\alpha_l \gamma_l P_{\infty,l}}{\gamma_l - 1} + \dfrac{\alpha_g \gamma_g P_{\infty,g}}{\gamma_g - 1}. \end{cases} \tag{3.8}$$

The sound speed of the mixture (C), which will be needed by the numerical solver discussed later in § 4 as a characteristic speed, is constructed in a similar way as in Allaire *et al.* (2002):

$$\frac{\rho C^2}{\gamma - 1} = \frac{\alpha_l \rho_l C_l^2}{\gamma_l - 1} + \frac{\alpha_g \rho_g C_g^2}{\gamma_g - 1}. \tag{3.9}$$

https://doi.org/10.1017/jfm.2026.11808 Published online by Cambridge University Press

This formulation guarantees that the sound speed monotonically transits from one phase to the other across the diffuse interface region in the present work.

3.4. *Fluxes and sources in the diffuse interface region*

To complete (3.1), the energy fluxes and sources for the mixture (i.e. $\boldsymbol{q}$, $\boldsymbol{F}_r$ and S_r) need to be formulated, in addition to the EOS. Furthermore, their expressions must satisfy the jump conditions described in § 3.1, i.e. these quantities vanish at the interfaces.

To obtain physically reasonable expressions for S_r and $\boldsymbol{q}$ in the mixture energy equation (3.1), we start with the separate energy equation for each phase:

$$\partial_t\left(\rho_l\alpha_l e_l\right)+\boldsymbol{\nabla}\cdot\left(\rho_l\alpha_l e_l\boldsymbol{u}\right)+\alpha_l p\,\boldsymbol{\nabla}\cdot\boldsymbol{u}=-\boldsymbol{\nabla}\cdot\left(\boldsymbol{q}_{ll}+\boldsymbol{q}_{lg}\right)+S_{r,l}+Q_{lg},\tag{3.10}$$

$$\partial_t\left(\rho_g\alpha_g e_g\right)+\boldsymbol{\nabla}\cdot\left(\rho_g\alpha_g e_g\boldsymbol{u}\right)+\alpha_g p\,\boldsymbol{\nabla}\cdot\boldsymbol{u}=-\boldsymbol{\nabla}\cdot\left(\boldsymbol{q}_{gl}+\boldsymbol{q}_{gg}\right)+S_{r,g}+Q_{gl},\tag{3.11}$$

where the fluxes and source for the liquid are retained at this moment without losing generality; in other words, the liquid is also treated as a kind of plasma. Note that energy exchanges occur both within and between phases. Here, $\boldsymbol{q}_{ij}$ $(i,\,j\in\{l,\,g\})$ denotes the thermal energy flux across the interface of any infinitesimal control volume, carried by the surrounding phase j and applied to the internal phase i, $S_{r,i}$ $(i\in\{l,\,g\})$ is the radiation energy deposition rate to phase i, and Q_{ij} $(i,\,j\in\{l,\,g\},\ \ i\neq j)$ is the energy exchange rate from internal phase j to internal phase i with $Q_{lg}=-Q_{gl}$. For generality, we initially retain all terms for the liquid phase, effectively treating it as a plasma with its own transport coefficients – the thermal conductivity λ_l, the radiative energy exchange rate $\omega_{r,l}$, and the radiative energy diffusion coefficient $\chi_{r,l}$ – despite these being typically much smaller than their plasma-phase counterparts.

The radiative energy source for each phase is modelled as

$$S_{r,i}=\alpha_i\omega_{r,i}\left(T_r^4-T_i^4\right),\quad\ i\in\{l,\,g\}.\tag{3.12}$$

Therefore the source of the mixture is the sum of $S_{r,g}$ and $S_{r,l}$, which reads

$$S_r=\alpha_g\omega_{r,g}\left(T_r^4-T_g^4\right)+\alpha_l\omega_{r,l}\left(T_r^4-T_l^4\right).\tag{3.13}$$

According to its definition, the plasma-to-plasma conductive heat flux $\boldsymbol{q}_{gg}$ should be proportional to the local area over which the internal plasma contacts the surrounding plasma. For a homogeneous mixture of plasma and liquid, the local fraction of contact area between the plasmas is equal to the product of the volume fractions on both sides, namely $\alpha_g^+\alpha_g^-$, where the superscripts $+$ and $-$ denote the internal and external sides of the contact surface, respectively. Given homogeneity, $\alpha_g=\alpha_g^+=\alpha_g^-$ and $\alpha_l=\alpha_l^+=\alpha_l^-$. Therefore, we can have

$$\boldsymbol{q}_{gg}=-\alpha_g^2\lambda_g\boldsymbol{\nabla}T_g.\tag{3.14}$$

Similarly, the contact area fraction between the internal plasma and the surrounding liquid can be expressed as $\alpha_g^+\alpha_l^-$. The interphase thermal conduction is expected to be determined by the two phases, thus we phenomenologically assign the effective interphase thermal conduction coefficient as $\sqrt{\lambda_g\lambda_l}$, a geometric average of λ_g and λ_l. Assuming a local temperature difference $T_g^+-T_l^-$ over a small length scale $\delta\boldsymbol{x}$, the liquid-to-plasma flux $\boldsymbol{q}_{gl}$ can be estimated by

$$\boldsymbol{q}_{gl}=-\alpha_g^+\alpha_l^-\sqrt{\lambda_g\lambda_l}\left(T_g^+-T_l^-\right)/\delta\boldsymbol{x}.\tag{3.15}$$

https://doi.org/10.1017/jfm.2026.11808 Published online by Cambridge University Press

Equation (3.15) can be reformulated in two equivalent ways:

$$\begin{aligned}\boldsymbol{q}_{gl} &= -\alpha_g^+\alpha_l^-\sqrt{\lambda_g\lambda_l}\left(\nabla T_g + \left(T_g^- - T_l^-\right)/\delta\boldsymbol{x}\right), \qquad \text{or}\\ &= -\alpha_g^+\alpha_l^-\sqrt{\lambda_g\lambda_l}\left(\nabla T_l + \left(T_g^+ - T_l^+\right)/\delta\boldsymbol{x}\right).\end{aligned} \tag{3.16}$$

In these forms, the local temperature difference between the plasma and liquid phases ($T_g^+ - T_l^+$ or $T_g^- - T_l^-$) implies that $\boldsymbol{q}_{gl}$ is also related to the exchange rate of internal energy from plasma to liquid, Q_{gl}, evaluated on the internal and external sides of the contact surface, respectively.

To keep the notational symmetry, the liquid-to-liquid and plasma-to-liquid energy fluxes due to thermal conduction can be expressed as

$$\boldsymbol{q}_{ll} = -\alpha_l^2\lambda_l\nabla T_l, \quad \boldsymbol{q}_{lg} = -\alpha_l^+\alpha_g^-\sqrt{\lambda_g\lambda_l}\left(T_l^+ - T_g^-\right)/\delta\boldsymbol{x}. \tag{3.17}$$

The mixture thermal flux is then contributed by all of the fluxes within and between phases, i.e. $\boldsymbol{q} = \boldsymbol{q}_{gg} + \boldsymbol{q}_{gl} + \boldsymbol{q}_{lg} + \boldsymbol{q}_{ll}$. It is worth noting that the temperature differences between the plasma and liquid phases in $\boldsymbol{q}_{lg}$ and $\boldsymbol{q}_{gl}$ cancel upon summation. Consequently, the final expression for $\boldsymbol{q}$ can be simplified accordingly:

$$\boldsymbol{q} = -\alpha_g^2\lambda_g\nabla T_g - \alpha_g\alpha_l\sqrt{\lambda_g\lambda_l}\,(\nabla T_g + \nabla T_l) - \alpha_l^2\lambda_l\nabla T_l. \tag{3.18}$$

This modelling approach has the desirable property that it reduces to Fick's law $\boldsymbol{q} = -\lambda\nabla T$ in the limit where the two phases are identical, thereby ensuring its consistency with the single-phase theory.

The energy flux due to radiation diffusion is analogous to the conductive heat flux to some degree. In the optically thick limit, where the radiation can be described as a diffusion field, the radiation diffusion fluxes are proportional to the contact area between phases and the respective radiation diffusion coefficients ($\chi_{r,g}$, $\chi_{r,l}$). By direct analogy to the conductive heat flux form derived in (3.18), the radiation energy flux for the mixture can be written as

$$\boldsymbol{F}_r = -(\alpha_g^2\chi_{r,g} + 2\alpha_g\alpha_l\sqrt{\chi_{r,g}\chi_{r,l}} + \alpha_l^2\chi_{r,l})\,\nabla T_r^4. \tag{3.19}$$

Because of the comparatively negligible thermal conduction coefficient and high opacity of the liquid, we set $\lambda_l \approx 0$, $\omega_{r,l} \approx 0$ and $\chi_{r,l} \approx 0$ in this paper. Accordingly, the radiative energy source, the conductive heat flux and the radiative diffusion flux yields a simplified model valid within the diffuse interface region:

$$\begin{cases}\boldsymbol{q} = -\alpha_g^2\lambda_g\nabla T_g,\\ S_r = \alpha_g\omega_{r,g}\left(T_r^4 - T_g^4\right),\\ \boldsymbol{F}_r = -\alpha_g^2\chi_{r,g}\nabla T_r^4.\end{cases} \tag{3.20}$$

This simplified formulation preserves a continuous transition for the energy fluxes and sources from the plasma to the liquid, governed by the plasma volume fraction α_g. At the same time, it satisfies the required jump conditions at the interfaces.

3.5. *Summary of the model for plasma–liquid interactions*

By applying the expressions of the energy fluxes and source in (3.20), we now rewrite the radiation two-phase flow model in (3.1) as

https://doi.org/10.1017/jfm.2026.11808 Published online by Cambridge University Press

$$\begin{cases} \partial_t \alpha_l + \boldsymbol{u} \cdot \nabla \alpha_l = 0, \\ \partial_t (\rho_l \alpha_l) + \nabla \cdot (\rho_l \alpha_l \boldsymbol{u}) = 0, \\ \partial_t (\rho_g \alpha_g) + \nabla \cdot (\rho_g \alpha_g \boldsymbol{u}) = 0, \\ \partial_t (\rho \boldsymbol{u}) + \nabla \cdot (\rho \boldsymbol{u}\boldsymbol{u}) + \nabla \cdot ((p + p_r)\boldsymbol{I}) = \sigma \kappa \nabla \phi, \\ \partial_t (\rho e) + \nabla \cdot (\rho e \boldsymbol{u}) + p \nabla \cdot \boldsymbol{u} = \nabla \cdot \left(\alpha_g^2 \lambda_g \nabla T_g\right) + \alpha_g \omega_{r,g} \left(T_r^4 - T_g^4\right), \\ \partial_t E_r + \nabla \cdot (E_r \boldsymbol{u}) + p_r \nabla \cdot \boldsymbol{u} = \nabla \cdot \left(\alpha_g^2 \chi_{r,g} \nabla T_r^4\right) - \alpha_g \omega_{r,g} \left(T_r^4 - T_g^4\right). \end{cases} \tag{3.21}$$

Although this model is derived for the mixture, it exhibits the correct asymptotic behaviour by reducing to standard single-phase models in the limit of α_g. It is straightforward that the system of equations in (3.21) converges to the Euler equation (2.3) for the pure liquid in the limit of vanishing plasma and radiation, while it recovers the RHD equations for a pure plasma (2.1) as $\alpha_g \to 1$.

4. Numerical method

In order to numerically solve the radiation two-phase flow for plasma–liquid interactions described in (3.21), we employ an operator-splitting numerical algorithm (McLachlan & Quispel 2002). This approach is particularly effective for handling the multiphysics nature of the equations, where the characteristic time scales and numerical stiffnesses associated with convective transport differ significantly from those of diffusive processes. The method proceeds by separating the full system into two sequential sub-problems – a hyperbolic step and a parabolic step – and consequently allows us to use efficient numerical techniques to account for the distinct mathematical properties of each sub-problem.

In the hyperbolic step, we integrate the subsystem governing convection of the fluid and radiation. Note that the energy equations for fluid and radiation convection of (3.21) are not in the conservative form, primarily due to the pressure–work terms associated with fluid compressibility. In order to impose strict energy conservation, we instead consider the convection of the total energy density ρe_t, which is defined as $\rho e_t = \rho e + E_r + \rho |\boldsymbol{u}|^2 / 2$. The governing equations for the hyperbolic system are

$$\partial_t \alpha_l + \nabla \cdot (\alpha_l \boldsymbol{u}) = \alpha_l \nabla \cdot \boldsymbol{u}, \tag{4.1a}$$

$$\partial_t (\rho_l \alpha_l) + \nabla \cdot (\rho_l \alpha_l \boldsymbol{u}) = 0, \tag{4.1b}$$

$$\partial_t (\rho_g \alpha_g) + \nabla \cdot (\rho_g \alpha_g \boldsymbol{u}) = 0, \tag{4.1c}$$

$$\partial_t (\rho \boldsymbol{u}) + \nabla \cdot (\rho \boldsymbol{u}\boldsymbol{u}) + \nabla \cdot (p_t \boldsymbol{I}) = \sigma \kappa \nabla \phi, \tag{4.1d}$$

$$\partial_t (\rho e_t) + \nabla \cdot (\rho e_t \boldsymbol{u}) + \nabla \cdot (p_t \boldsymbol{u}) = \sigma \kappa \nabla \phi \cdot \boldsymbol{u}, \tag{4.1e}$$

with the total pressure given by $p_t = p + p_r$. Equation (4.1*e*) is obtained by summing the energy equation of the fluid and radiation (3.21), and the dot product of (4.1*d*) with the velocity vector; further details are provided in Appendix A.

In the parabolic step, we integrate the subsystem governing thermal conduction and radiation diffusion:

$$\begin{cases} \partial_t (\rho e) = \nabla \cdot \left(\alpha_g^2 \lambda_g \nabla T_g\right) + \alpha_g \omega_{r,g} \left(T_r^4 - T_g^4\right), \\ \partial_t E_r = \nabla \cdot \left(\alpha_g^2 \chi_{r,g} \nabla T_r^4\right) + \alpha_g \omega_{r,g} \left(T_g^4 - T_r^4\right). \end{cases} \tag{4.2}$$

In particular, an explicit scheme is implemented for the convection of fluid and radiation, with an implicit scheme for the thermal conduction and radiation diffusion; details

https://doi.org/10.1017/jfm.2026.11808 Published online by Cambridge University Press

are provided in the following subsections. Both the explicit scheme for (4.1) and the implicit scheme for (4.2) are embedded in a second-order Runge–Kutta scheme for time integration.

4.1. *Hyperbolic step: convection of fluid and radiation*

The convection equations (4.1) are discretised using a second-order finite-volume scheme with the numerical fluxes computed via the HLLC approximate Riemann solver (Toro 2013). The characteristic wave speed C_s is obtained from the eigenvalue of the hyperbolic system, computed from its Jacobian matrix; see Appendix B for details. The term for velocity divergence in the volume-fraction advection equation (4.1*a*) is evaluated using the adapt-HLLC scheme (Johnsen & Colonius 2006). The surface tensions in (4.1*d*) and (4.1*e*) are treated as source terms and discretised by the central difference scheme. The time step Δt is chosen adaptively such that the Courant–Friedrichs–Lewy (CFL) condition is strictly satisfied:

$$\Delta t = \mathrm{CFL} \times \min_{i \in D} \left\{ \frac{\sqrt[3]{V_i}}{|\boldsymbol{u}_i| + C_{s,i}} \right\}, \tag{4.3}$$

where the CFL number ($=0.44$) is a prescribed constant, the subscript i denotes a Cartesian cell in the computational domain D, $C_s = \sqrt{C^2 + 4p_r/(3\rho)}$ is the local wave speed, and V is the volume of the cell.

After solving the fluid and radiation convection explicitly, we update the conservative variables to an intermediate state, denoted by the superscript $*$: $[\alpha_l^*, (\rho_l\alpha_l)^*, (\rho_g\alpha_g)^*, (\rho\boldsymbol{u})^*, (\rho e_t)^*]^{\mathrm{T}}$. The corresponding primitive variables at the intermediate state are also updated. From $(\rho e_t)^*$, the internal energy $(\rho e)^*$ and radiation energy $(E_r)^*$ of the mixture can then be calculated; see details in Appendix C.

4.2. *Parabolic step: thermal conduction and radiation diffusion*

An implicit scheme is adopted for the time integration of the thermal conduction and radiation diffusion in (4.2). All the coefficients in the equations are linearised using the flow variables at the intermediate state:

$$\begin{cases} \dfrac{(\rho e)^{n+1} - (\rho e)^*}{\Delta t} = \nabla \cdot \left(\left(\alpha_g^2 \lambda_g\right)^* \nabla (T_g)^{n+1} \right) + (\alpha_g \omega_{r,g})^* \left(T_r^4 - T_g^4\right)^{n+1}, \\ \dfrac{(E_r)^{n+1} - (E_r)^*}{\Delta t} = \nabla \cdot \left(\left(\alpha_g^2 \chi_{r,g}\right)^* \nabla \left(T_r^4\right)^{n+1} \right) + (\alpha_g \omega_{r,g})^* \left(T_g^4 - T_r^4\right)^{n+1}. \end{cases} \tag{4.4}$$

The gradient and divergence terms are discretised using a central finite-difference scheme. By solving (4.4) iteratively, ρe and E_r are updated from the intermediate state to the $n+1$ time step. Subsequently, by employing the EOS, all remaining conservative and primitive variables associated with energy, such as p, p_r, T_g and T_r, are calculated for the $n+1$ time step, while those related to mass and momentum are retained from the intermediate state. This completes the numerical solution of the radiation two-phase flow system for plasma–liquid interactions.

5. Model validations

In this section, we validate the radiation two-phase flow model by simulating two types of flows: plasma single-phase flow and liquid–gas two-phase flow. The numerical results for each are compared against benchmark solutions from the literature.

https://doi.org/10.1017/jfm.2026.11808 Published online by Cambridge University Press

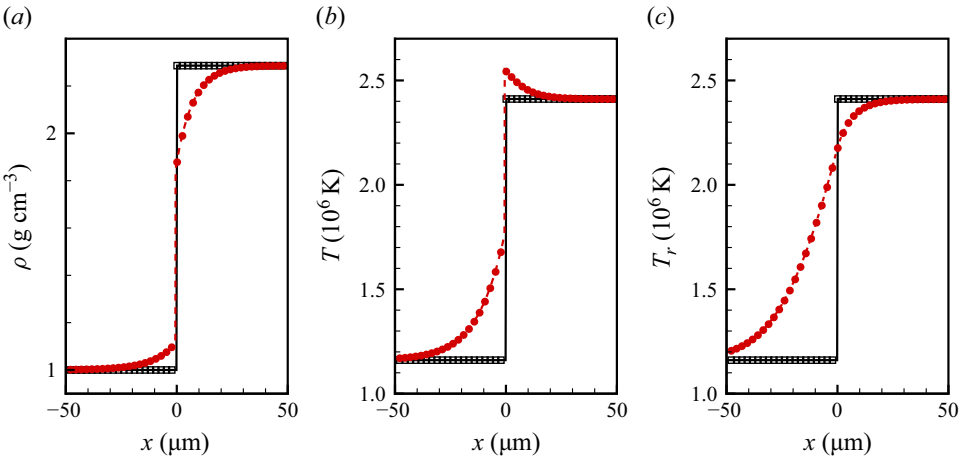


Figure 2. The profiles of a radiative shock problem at 0 ns (black solid lines and open squares) and 4.2 ns (red dashed lines and solid circles), in terms of (*a*) density, (*b*) plasma temperature, and (*c*) radiation temperature. The symbols and lines denote numerical and semi-analytical solutions, respectively. Note that the symbols are sampled at every 8th grid point for visual clarity.

5.1. *Radiative shock tube*

To validate the radiation transport in our model, we consider a one-dimensional radiative shock tube problem, where the radiation energy fluxes and radiation pressure significantly affect the hydrodynamics. As illustrated in figure 2, a low-temperature low-density plasma (with density ρ^L, temperature T^L and velocity u^L) is initially impacting a high-temperature high-density plasma (with density ρ^R, temperature T^R and velocity u^R). This configuration is designed to produce a stationary radiative shock at $x = 0\,\mu\text{m}$, the solution of which can be compared with the semi-analytical result from Lowrie & Edwards (2008).

Because the fluid system only has one phase, i.e. plasma, we set $\alpha_g = 1$ everywhere in the domain. The properties of the plasma are an adiabatic index $\gamma_g = 5/3$, a molar mass $M_g = 2\ \text{g mol}^{-1}$, and a constant ionisation degree $Z_g = 1$, which determine $c_{v,g} = 1.247 \times 10^8\ \text{cm}^2\ \text{s}^{-2}\ \text{K}^{-1}$. Thermal conduction is neglected (i.e. $\lambda_g = 0$). The diffusion coefficient and the exchange rate of the radiative energy are $\chi_{r,g} = 1.268 \times 10^7\ \text{cm}^2\ \text{s}^{-1}$ and $\omega_{r,g} = 1.268 \times 10^{13}\ \text{s}^{-1}$, respectively. The initial conditions are defined by a step function at $x = 0\,\mu\text{m}$, as illustrated in figure 2. The radiation is initially set in thermal equilibrium with the plasma (i.e. $T_r = T$). The initial flow parameters of the plasma are

$$\begin{cases} \rho^R = 2.286\ \text{g cm}^{-3}, \quad T^R = 2.411 \times 10^6\ \text{K}, \quad u^R = 1.11 \times 10^7\ \text{cm s}^{-1}, \\ \rho^L = 1\ \text{g cm}^{-3}, \quad T^L = 1.16 \times 10^6\ \text{K}, \quad u^L = 2.536 \times 10^7\ \text{cm s}^{-1}. \end{cases} \tag{5.1}$$

The computation is performed in a domain $[-300,\ 300]\,\mu\text{m}$, discretised by a uniform grid of 2000 points.

Figure 2 presents numerical results at $t = 4.2$ ns in terms of density, plasma temperature and radiation temperature. These results are superimposed with the semi-analytical solution by Lowrie & Edwards (2008). Obviously, the numerical results are in excellent agreement with the theoretical prediction, with respect to the position of the stationary shock and the diffusion profiles on either side of the discontinuity. The comparison demonstrates that the proposed model can be reduced to an RHD model for single phase, and successfully captures complex plasma flow structures, including radiative shocks.

https://doi.org/10.1017/jfm.2026.11808 Published online by Cambridge University Press

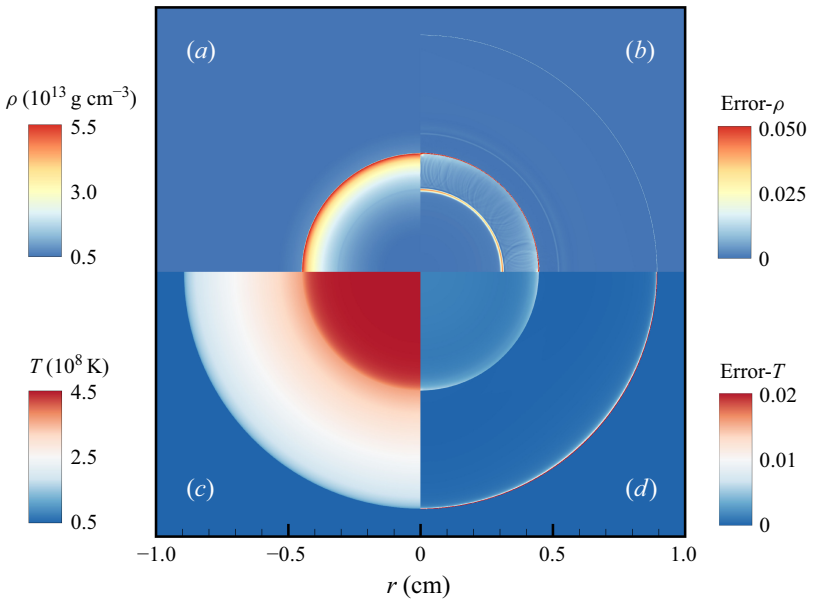


Figure 3. (*a*) Density, (*b*) relative density error $|\rho^N - \rho^A|/\rho^A$, (*c*) temperature, and (*d*) relative temperature error $|T^N - T^A|/T^A$ for the Reinicke–Meyer-ter-Vehn blast wave problem at 0.52 ns, where superscripts N and A represent numerical and semi-analytical results, respectively.

5.2. *Blast wave with thermal conduction*

To validate the thermal conduction in our model, we consider the Sedov–Taylor point explosion with nonlinear thermal conduction, also referred to as the Reinicke–Meyer-ter-Vehn problem, which only involves the plasma phase and has the semi-analytical solution for the blast wave (Reinicke & Meyer-ter-Vehn 1991). To avoid the singularity of a point explosion, the initial condition for the simulation is taken from the semi-analytical solution right after the bang time. At this moment, the stationary and uniform ambient plasma is about to be swept through by a tiny and rapidly expanding spherical blast wave.

The plasma is modelled as an ideal gas with adiabatic index $\gamma_g = 1.25$, molar mass $M_g = 1\ \mathrm{g\,mol^{-1}}$ and ionisation degree zero, giving a specific heat capacity at constant volume $c_{v,g} = 3.326 \times 10^8\ \mathrm{cm^2\ s^{-2}\ K^{-1}}$. The radiation transport is not excluded from this problem; accordingly, the radiation energy E_r, the radiation pressure p_r, the radiative energy exchange rate $\omega_{r,g}$, and the radiative energy diffusion coefficient $\chi_{r,g}$ for the plasma are all set to zero. The thermal conduction coefficient follows a nonlinear power-law function of density and temperature as recommended by Reinicke & Meyer-ter-Vehn (1991), i.e. $\lambda_g = \rho_g^{-2} T_g^{6.5}$ (in $\mathrm{g\,cm\,s^{-3}\,K^{-1}}$), where ρ_g is in $\mathrm{g\,cm^{-3}}$, and T_g is in K. Axisymmetric simulations are performed in 2-D cylindrical coordinates ((r, z) plane). The initial condition corresponds to the semi-analytical solution at $t = 0.2$ ns, when the shock front has radius 0.225 cm, and the heat front has radius 0.45 cm. The computational domain is $[0, 1] \times [0, 1]\ \mathrm{cm^2}$, and is discretised by 2048×2048 grid points.

Figures 3(*a*) and 3(*c*) illustrate the distributions of density and temperature at $t =$ 0.52 ns. As predicted by Reinicke & Meyer-ter-Vehn (1991), the shock front reached radius 0.45 cm and the heat front 0.9 cm. The corresponding relative errors in density and temperature are shown in figures 3(*b*) and 3(*d*), respectively. The maximum errors, which do not exceed 5 %, are localised at the discontinuities of the shock and heat front, and are attributed to finite grid resolution. The good agreement with the semi-analytical solution

https://doi.org/10.1017/jfm.2026.11808 Published online by Cambridge University Press

demonstrates the capability of the proposed model to accurately deal with nonlinear thermal conduction.

5.3. *Bubble collapse induced by shock wave*

The shock-induced collapse of a gas bubble in water, where a planar shock wave propagating through the water interacts with an underwater gas bubble, has been extensively studied by simulations (Nourgaliev, Dinh & Theofanous 2006; Hawker & Ventikos 2012; Bo & Grove 2014). This classic problem is used here to verify that the governing equations of the proposed model correctly reduce to those for compressible two-phase flows. In this case, thermal conduction, radiation transport and surface tension are neglected. Consequently, all associated variables and coefficients – including radiation energy E_r, radiation pressure p_r, thermal conduction coefficient λ_g, radiative energy diffusion coefficient $\chi_{r,g}$, radiative energy exchange rate $\omega_{r,g}$, and surface tension coefficient σ – are set to zero. Regarding the EOS, the water is described by the SG model (parameters are listed in table 1), while the gas phase is treated as an ideal gas with $\gamma_g = 1.4$.

The simulation is performed in 2-D Cartesian coordinates. Initially, a circular bubble is centred at (0, 0) mm with radius 3 mm. The density and pressure inside the bubble are 1 kg m^{-3} and 10^5 Pa, respectively. An incident shock wave is positioned at 5.4 mm to the left of the bubble centre initially, and propagates to the $x+$ direction. The right-hand (with the superscript R) and left-hand (with the superscript L) sides of the shock are initialised as follows:

$$\begin{cases} \rho^R = 1000\ \text{kg m}^{-3}, \quad p^R = 10^5\ \text{Pa}, \quad u^R = 0, \\ \rho^L = 1323.65\ \text{kg m}^{-3}, \quad p^L = 1.9 \times 10^9\ \text{Pa}, \quad u^L = 681.58\ \text{m s}^{-1}. \end{cases} \tag{5.2}$$

The computational domain spans $[-15, 15] \times [-15, 15]$ mm^2, and the bubble radius (3 mm) is initially discretised by 800 grid points.

Figure 4 demonstrates different stages of the shock-induced bubble collapse in the simulation, visualised by pressure contours and numerical schlieren. Upon shock impact, a reflected rarefaction wave forms in the liquid, and a transmitted shock develops inside the bubble, as shown in figure 4(*a*). At the same time, a re-entrant liquid jet forms at the left-hand side of the bubble, and propagates in the same direction as the incident shock, as shown in figure 4(*b*). Upon impact of the jet with the rear interface of the bubble, a water-hammer shock is generated (see e.g. $t = 3.9\,\mu$s in figure 4*c*). The characteristic parameters of this event include the collision time t_c, the water-hammer shock pressure p_w, and the jet speed v_j at the instant of impact. Subsequently, the jet penetrates the bubble and merges with the surrounding liquid, while secondary jets gradually develop (see figure 4*d*). These flow features closely resemble the numerical results reported in Hawker & Ventikos (2012). A quantitative comparison on t_c, v_j and p_w with the literature is provided in table 2. Good agreement is achieved for t_c and v_j, while p_w is relatively lower in the present simulation, primarily due to coarser spatial resolution. The results confirm that the proposed radiation two-phase flow model correctly reduces to a standard compressible two-phase flow formulation when the radiation-specific terms are disabled. Furthermore, the good agreement with expected flow dynamics validates the core flow solver and the implementation of the EOS before the coupling with radiation transport and thermal conduction is introduced.

https://doi.org/10.1017/jfm.2026.11808 Published online by Cambridge University Press

	t_c (μs)	v_j (m s^{-1})	p_w (GPa)
Present	3.70	2837	5.03
Lin *et al.* (2017)	3.70	2832	5.90
Hawker & Ventikos (2012)	3.66	2810	5.89
Bo & Grove (2014)	3.70	2830	—
Nourgaliev *et al.* (2006)	3.69	2850	10.1

Table 2. Shock-induced bubble collapse compared to prior simulations: collision time (t_c), jet speed at collision (v_j), and water-hammer shock pressure (p_w).

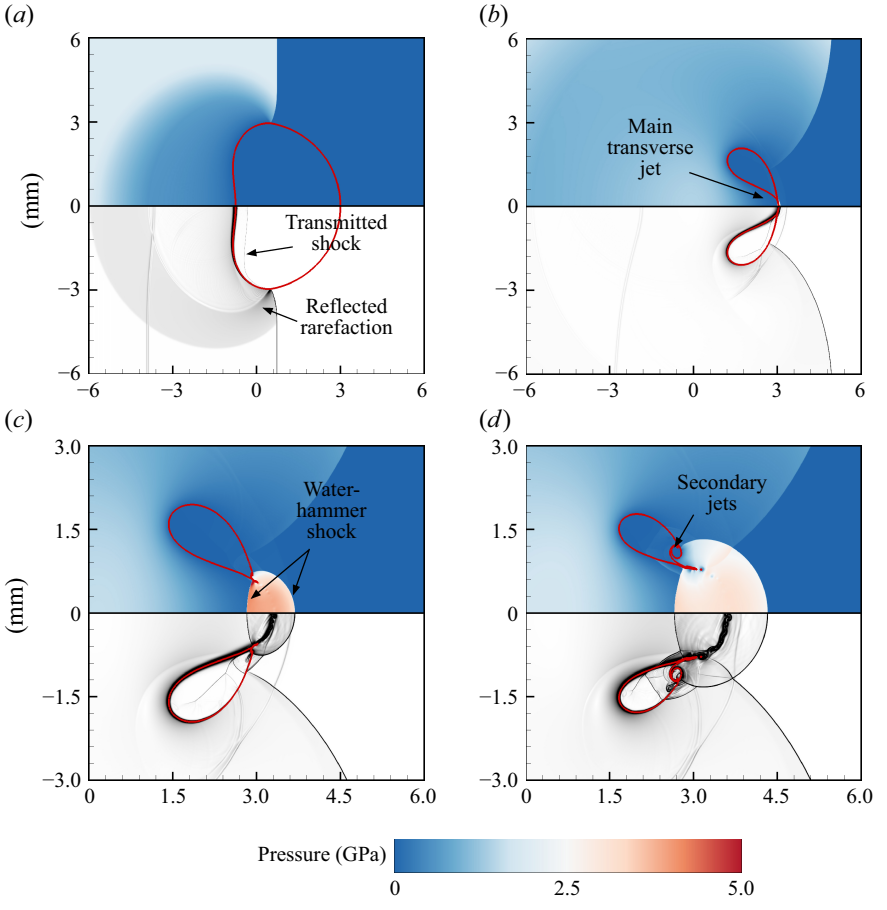


Figure 4. Numerical results of bubble collapse induced by a planar shock with respect to pressure (upper half) and numerical schlieren (lower half) at (*a*) 2.2 μs, (*b*) 3.7 μs, (*c*) 3.9 μs, (*d*) 4.1 μs. The red lines represent the bubble interfaces (by $\alpha_g = 0.5$).

5.4. *Droplet oscillation driven by surface tension*

Due to the imbalance in surface tension, an initially elliptical droplet oscillates periodically, converting between potential and kinetic energy (Garrick *et al.* 2017). The

https://doi.org/10.1017/jfm.2026.11808 Published online by Cambridge University Press

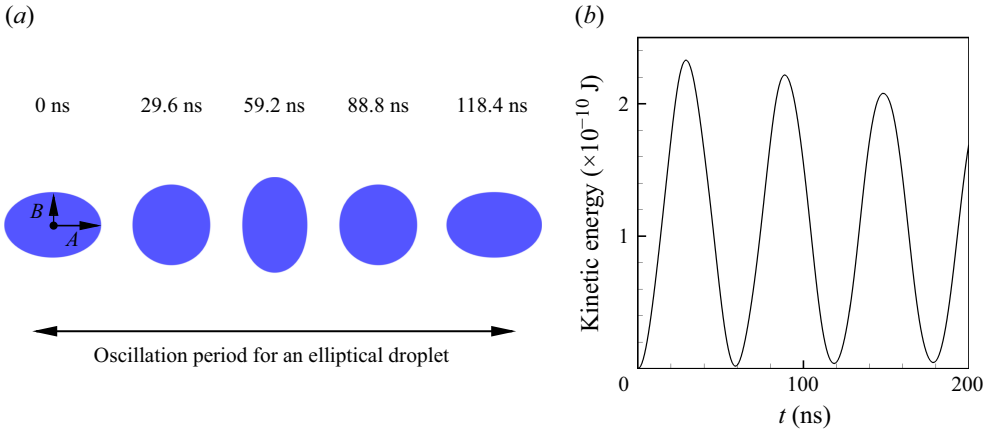


Figure 5. Droplet oscillation: (*a*) evolution of the droplet over an oscillation period, where A and B denote the initial semi-axes; (*b*) kinetic energy of the droplet.

oscillation period can be analytically obtained (Fyfe, Oran & Fritts 1988):

$$t_{os} = 2\pi\sqrt{\frac{(\rho_l + \rho_g)R^3}{(o^3 - o)\sigma}}, \tag{5.3}$$

where o is the oscillation mode, and R is the radius of the droplet at equilibrium. We employ this case to validate the surface tension model.

In the droplet oscillation, thermal conduction and radiation transport are absent; therefore, all corresponding variables and coefficients (E_r, p_r, λ_g, $\chi_{r,g}$, $\omega_{r,g}$) are set to zero in the simulation. For the EOS, the droplet is modelled as water by the SG model (see table 1), while the gas phase is treated as an ideal gas with $\gamma_g = 1.33$. The surface tension coefficient of the droplet is fixed at $\sigma = 500\ \mathrm{mN\,m^{-1}}$. The simulation is performed in 2-D Cartesian coordinates. Initially, the elliptical droplet is centred at (0, 0) μm with the semi-axes $A = 1.2\ \mu\mathrm{m}$ and $B = 0.8\ \mu\mathrm{m}$, resulting in droplet radius $R = 0.9798\ \mu\mathrm{m}$ at equilibrium. The initial pressure of both the droplet and the ambient gas is set at 1.3×10^5 Pa, while the densities of the two phases are $1073.55\ \mathrm{kg\,m^{-3}}$ and $0.74\ \mathrm{kg\,m^{-3}}$, respectively. To exploit symmetry of the oscillation, only a quarter of the physical domain ($[0, 5] \times [0, 5]\ \mu\mathrm{m}^2$) is simulated, with uniform mesh resolution 2 nm.

Figure 5(*a*) shows snapshots of the droplet shapes at different times over one oscillation period, corresponding to the phase values 0, $\pi/2$, π, $3\pi/2$ and 2π respectively. An oscillation mode $o = 2$ is observed. The periodicity of the droplet oscillation is quantitatively illustrated in figure 5(*b*), in terms of the kinetic energy ($\int (\rho_l \alpha_l\, |\boldsymbol{u}|^2\, /2)\, \mathrm{d}x\, \mathrm{d}y$) versus time. A gradual decay of the oscillation amplitude is observed due to numerical dissipation, consistent with the findings in other studies (Garrick *et al.* 2017; Long, Cai & Pan 2023). The oscillation period in simulation is 118.4 ns, with relative error 2.7 % compared to the theoretical prediction 115.3 ns. This demonstrates that the continuous surface tension incorporated in the present model accurately captures capillary effects.

6. Nanosecond laser pulse irradiates tin droplet

We use the proposed model to simulate an experimentally relevant pre-pulse scenario in LPP-EUV lithography, in which a tin droplet is irradiated by a nanosecond laser

https://doi.org/10.1017/jfm.2026.11808 Published online by Cambridge University Press

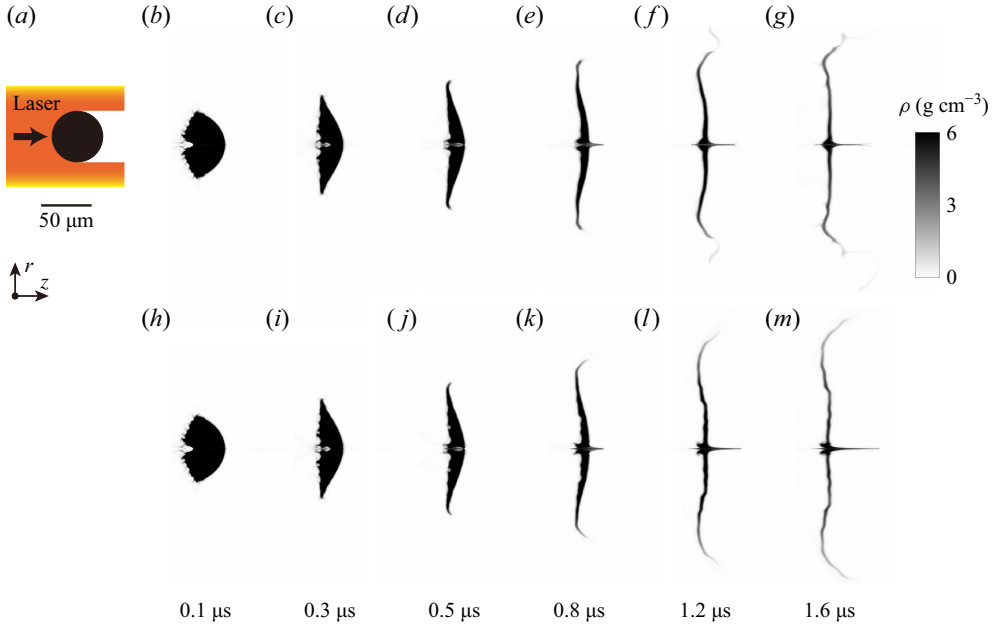


Figure 6. (*a*) Schematic of axisymmetric simulations of laser–droplet interactions. Cross-sectional shadowgraphs of the droplet at times ranging from $t = 0.1$ μs to $t = 1.6$ μs: (*b–g*) with surface tension, and (*h–m*) without surface tension. All images have the same spatial scale, as shown in (*a*).

pulse and deforms into a thin sheet. The simulation is configured as an axisymmetric case with parameters matched to the systematic experimental work of Kurilovich *et al.* (2016). The initial configuration is sketched in figure 6(*a*). Specifically, a 7 mJ Nd:YAG laser pulse with wavelength 1064 nm is employed, with duration 10 ns full width at half maximum (FWHM), and focal spot size 115 μm FWHM on the target, i.e. a tin ($\rho_l = 6.92$ g cm^{-3}) droplet with diameter $D = 50$ μm. The laser is modelled by using a ray-tracing approach, in which the beam is represented by over 20 000 individual rays that propagate geometrically through the plasma, each carrying a fraction of the total pulse energy. For this purpose, we adopt the ray-tracing methodology detailed in our earlier work (Tao *et al.* 2025). Energy deposition in the plasma occurs primarily through inverse bremsstrahlung absorption. This process depends on the local plasma temperature and electron number density, and is incorporated into the model as a space- and time-dependent source term on the right-hand side of the mixture energy equation in (3.21).

When the laser irradiates the tin droplet, plasma is generated via vaporisation and ionisation – processes not yet self-consistently included in the current model. A plasma layer is rapidly established surrounding the droplet, and blocks the laser from directly shining on the droplet surface, since a laser is unable to propagate beyond its critical density in a plasma (Kruer 1988). As a result, the laser energy is then deposited in the plasma only. To mimic the effects of phase change and plasma formation, we initialise a thin, high-density layer of ionised tin on the laser-irradiated (left-hand) surface of the droplet. The layer of high-density tin plasma is 1 μm thick, with density 1 g cm^{-3} on average, providing a simplified but typical representation of the initial plasma that absorbs incident laser energy. It is noteworthy that the mass of this layer that we initialise is consistent with experimental observations, i.e. less than 1 % of the droplet mass is ablated during the pre-pulse stage (Kurilovich *et al.* 2016).

https://doi.org/10.1017/jfm.2026.11808 Published online by Cambridge University Press

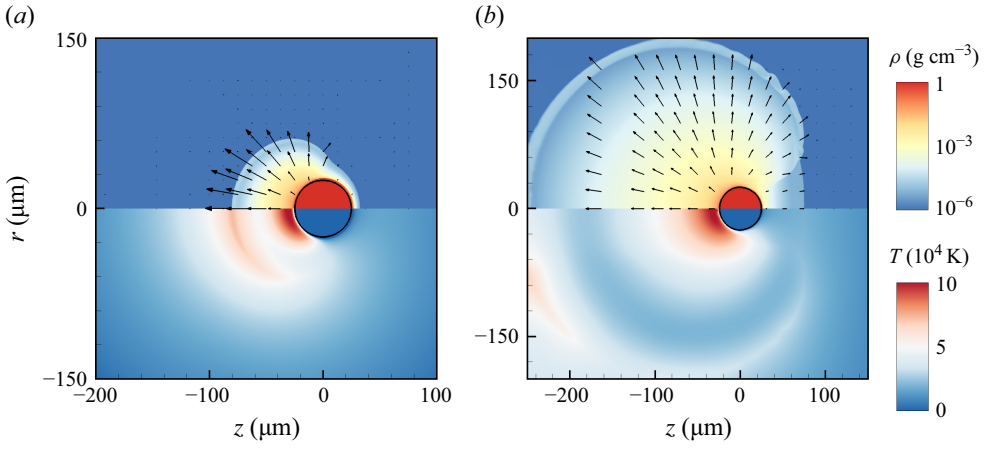


Figure 7. Numerical results of laser-droplet interaction at (*a*) 2 ns and (*b*) 10 ns, in terms of density (upper half) and temperature (lower half). The arrows denote velocity vectors, and the black lines represent the droplet shape (by $\alpha_l = 0.5$).

The tin droplet is modelled as an SG with the parameters listed in table 1 and the surface tension coefficient $\sigma = 538$ mN m^{-1}, while the tin plasma is treated as an ideal gas with $\gamma_g = 5/3$ and $M_g = 118.71$ g mol^{-1}. The ionisation degree (Z_g) is determined using the Thomas–Fermi model (More 1985), the thermal conduction coefficient (λ_g) follows the Spitzer–Härm theory (Spitzer & Härm 1953), and the radiative transport coefficients ($\chi_{r,g}$, $\omega_{r,g}$) are evaluated using the empirical formulae from Tsakiris & Eidmann (1987); see details in Appendix D. Radiation is initially set to be in thermal equilibrium with the materials. The computational domain spans [0, 300] μm in the radial direction (r), and [−300, 300] μm in the axial direction (z), and initially 400 grid points are used to resolve the droplet diameter.

Figure 7 shows the laser-induced plasma expansion at $t = 2$ ns and 10 ns during the laser–plasma interaction stage of the simulation. Under the left-hand side irradiation, the plasma expands rapidly, with the fastest motion occurring along the axial direction. The continuous laser energy deposition sustains a very high temperature ($\sim 10^5$ K) in the plasma near the irradiated surface of the droplet. The laser is absorbed below the critical density, and consequently forms a quasi-stationary ablation front, consistent with the simulations by Basko *et al.* (2015). In contrast, the droplet itself remains in a low-temperature, high-density liquid state, as illustrated by figure 7. Since the laser-pulse duration (10 ns) is much shorter than the inertial time scale of droplet dynamic response ($\sim D/U \approx 1$ μs, where U is the axial propulsion velocity taken from figure 10 below), the droplet shape has negligible deformation during the laser pulse. Significant deformation due to the high pressure at the ablation front is expected to occur on a longer time scale.

The in-flight deformation of the spherical droplet into a flat sheet over the inertial time scale is illustrated in figures 6(*b–g*). The deformation starts on the laser-irradiated (left) surface, where fine structures, resulting from the Rayleigh–Taylor instabilities induced by the LPP–droplet interaction, develop with time (see figure 6*b*). Subsequently, the droplet assumes a jellyfish-hat-like shape (figure 6*c*), and is gradually flattened and curves away from the direction of the laser beam (figures 6*d–g*). A notable feature during this flattening stage is the generation of an axial jet (figures 6*e–g*), consistent with the experimental observations (Klein *et al.* 2015, 2020; Meijer *et al.* 2022). It is remarkable that our proposed model successfully captures both this axial jet and the surficial fine structures,

https://doi.org/10.1017/jfm.2026.11808 Published online by Cambridge University Press

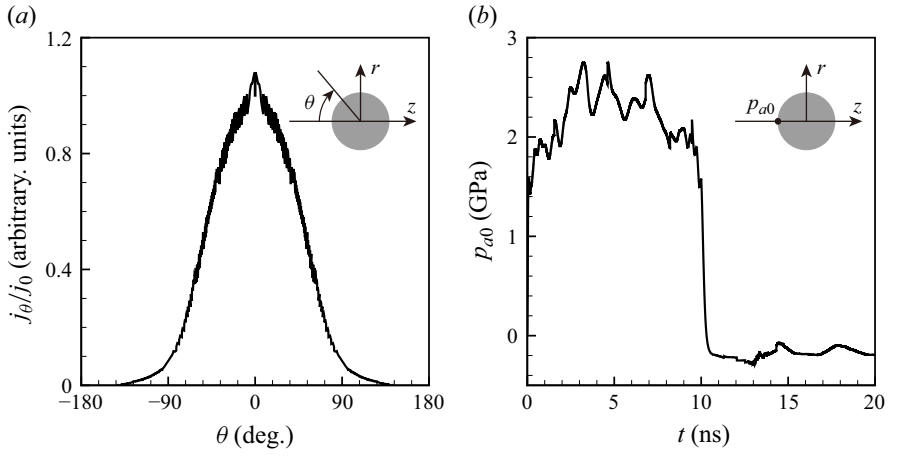


Figure 8. (*a*) Normalised surface impulse profiles: the simulation results. The inset shows the polar angle θ in the r–z coordinate. (*b*) Temporal evolution of the pressure exerted on the droplet surface at $\theta = 0$, p_{a0}.

which have rarely been reproduced in previous incompressible or single-phase RHD simulations. In addition, by comparing the droplet shape to the results obtained without surface tension (figures 6*h–m*), we observe that surface tension acts on a microsecond time scale, mildly smoothing small structures at the windward surface of the deformed droplet, and slightly suppressing the radial expansion of the liquid sheet.

During the laser–plasma interaction stage, the expanding plasma exerts on the droplet surface a very high ablation pressure that decays rapidly after the laser is turned off, in agreement with previous single-phase simulations (Kurilovich *et al.* 2018). The surface impulse arising from the ablation pressure can be defined as $j_\theta = \int_\tau p_a(t, \theta)\,\mathrm{d}t$, where $p_a(t, \theta)$ is the surface pressure, θ is the polar angle shown in figure 8(*a*), and the integration interval τ covers the laser-pulse duration (in this case $\tau = 10$ ns). This surface impulse model has been widely used (Gelderblom *et al.* 2016; Reijers *et al.* 2017; França *et al.* 2025) to assess the subsequent droplet deformation in the flattening stage, e.g. by serving as an input for the incompressible droplet simulations. Figure 8(*a*) displays the simulated profile of the normalised j_θ/j_0, where $j_0 = j_{\theta=0}$ is 21.9 Pa s. We note that the profile is characterised by a wide peak on the windward (from $-90°$ to $90°$), but a short tail on the leeward, resembling the so-called raised cosine pressure impulse (França *et al.* 2025), which has been suggested to account for the occurrence of curvature reversal under the incompressible framework (França *et al.* 2025). Despite this, our results demonstrate that the droplet deformation initiates on the laser side, then curves outwards at the radial edge, representing a qualitatively different morphological evolution from that predicted by the incompressible framework (França *et al.* 2025), in which the curvature reversal would start from deformation on the leeward side instead. Figure 8(*b*) shows the temporal evolution of the surface pressure p_a at $\theta = 0$, p_{a0}. During the laser irradiation, the value of p_{a0} ranges approximately from 1.5 GPa to 2.8 GPa, and its evolution exhibits multiple rises and drops, likely caused by pressure waves propagating across the ablation front.

Figure 9 shows the deformed droplet at $t = 0.4$ and 2 μs in terms of density contours. For direct comparison, the insets superimpose the projection outlines, obtained by azimuthally rotating the simulated droplet profiles, onto the corresponding experimental snapshots from Kurilovich *et al.* (2016). Clearly, excellent agreement has been achieved with respect to the droplet shapes. It should be pointed out that our axisymmetric simulations

https://doi.org/10.1017/jfm.2026.11808 Published online by Cambridge University Press

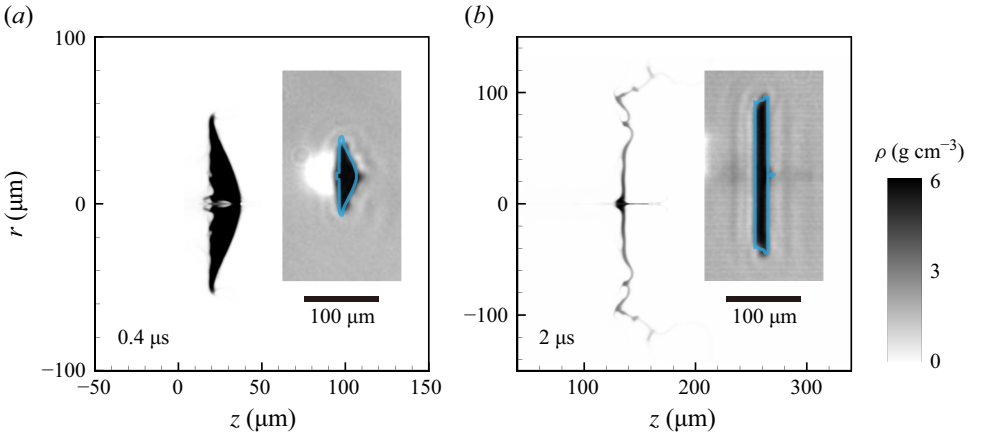


Figure 9. Density contours of the tin sheet at (*a*) 0.4 μs and (*b*) 2 μs. Insets show side-view experimental shadowgraphs (adapted from Kurilovich *et al.* 2016), superimposed on the simulated drop shape (with respect to the contour of $\rho = 1.2$ g cm^{-3}) representing the side-view projection.

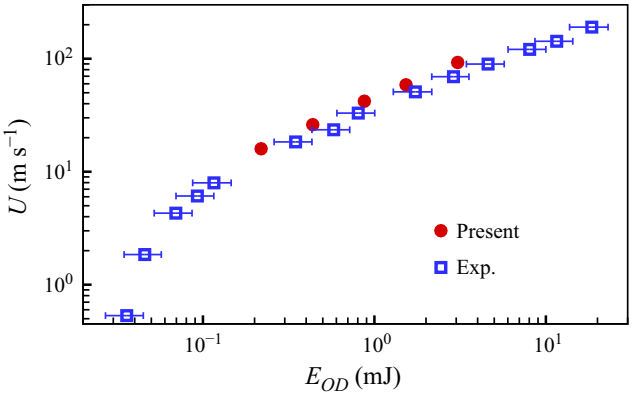


Figure 10. Propulsion velocity U of tin droplets as a function of total laser-pulse energy impinging on the droplet E_{OD}. The experimental data are taken from figure 3(*a*) of Kurilovich *et al.* (2016).

inherently cannot resolve three-dimensional (3-D) instabilities such as the Rayleigh–Plateau instabilities that would develop at the sheet's radial edge, leading to protruding ligaments and tiny droplets as observed in the experiments by Kharbedia *et al.* (2026). Similarly, the axisymmetric simulations cannot resolve 3-D Rayleigh–Taylor instabilities either, which have been proposed to account for sheet destabilisation and subsequent hole nucleation (Klein *et al.* 2020).

Figure 10 shows the axial propulsion velocity U of the tin sheets as a function of total laser-pulse energy impinging on the droplet E_{OD}, ranging from 0.22 to 3.06 mJ, while figure 11 illustrates the radial expansion of the tin droplets with two different laser energies as a function of time. Our numerical results show reasonably good quantitative agreement with the experimental data from Kurilovich *et al.* (2016), despite the use of the simplified models for EOS, thermal conduction, ionisation and radiation within the simulation. However, compared to the experimental observations, the radial expansion of the droplet is slightly overestimated, which is likely attributable to the prescribed plasma and numerical diffusion at the interface.

https://doi.org/10.1017/jfm.2026.11808 Published online by Cambridge University Press

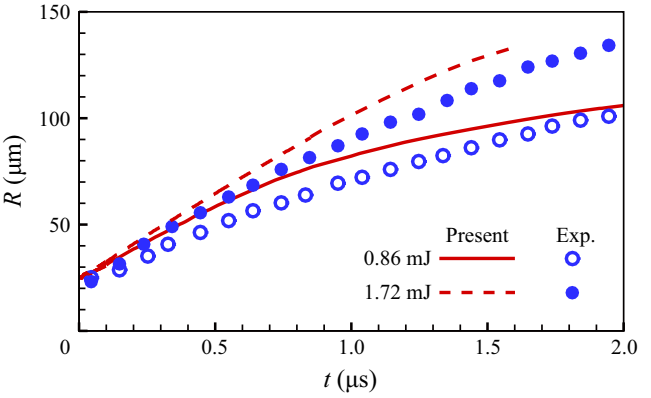


Figure 11. Radial expansion of tin droplets as functions of time with different laser-pulse energies: $E_{OD} = 0.86$ and 1.72 mJ. The experimental data are taken from figure 4(*a*) of Kurilovich *et al.* (2016).

7. Conclusion

We have developed a radiation two-phase flow model for plasma–liquid interactions using a diffuse interface framework. This approach approximates the physically sharp interface with a transition layer with finite thickness. Within this diffuse region, we formulated consistent energy flux closures that satisfy the correct physical jump conditions at the sharp interface limit, notably requiring the thermal and radiative energy fluxes from the plasma to vanish at the liquid surface. Additionally, appropriate EOS mixing rules were introduced to ensure the physical propagation of acoustic waves throughout the mixture. The model was advanced in time using an operator-splitting numerical algorithm, sequentially handling hyperbolic convection and parabolic diffusion. After comprehensive validation against three test cases from the literature, the model showed excellent performance for both single-phase plasma flows and liquid–gas two-phase flows. We then employed the proposed model to simulate an LPP-EUV relevant pre-pulse scenario: a tin droplet is irradiated by a nanosecond laser pulse, and deforms into a thin sheet. Our results show good agreement with the experimental findings of Kurilovich *et al.* (2016). The axisymmetric simulation successfully captures key experimentally observed features, such as the axial jet, that were rarely captured in previous simulations. Furthermore, it provides quantitatively accurate predictions of crucial dynamic properties, including the radial radius and axial propulsion velocity of the tin sheet.

By successfully simulating this complex LPP-EUV scenario, the proposed model establishes a framework for the self-consistent simulation of coupled laser–plasma physics and droplet dynamics. This framework enables systematic future studies of underlying mechanisms, such as the droplet propulsion, radial curvature reversal and axial jet formation. Moreover, the framework is well suited for incorporating additional essential physics, such as phase transition and more detailed material descriptions (e.g. tabulated EOS), thereby enabling fundamental studies of plasma–liquid interactions that are critical for the optimisation of state-of-the-art LPP-EUV sources.

Funding. We are grateful for the support of the National Natural Science Foundation of China (grant nos 12388101, 12375243), the Strategic Priority Research Programme of the Chinese Academy of Sciences (grant no. XDA0380601), and the Science Challenge Project (grant no. TZ2025016).

Declaration of interests. The authors report no conflict of interest.

https://doi.org/10.1017/jfm.2026.11808 Published online by Cambridge University Press

Appendix A. Governing equation for convection of the total energy density

The governing equation for the total energy ($\rho e_t = \rho e + E_r + \rho|\boldsymbol{u}|^2/2$) can be obtained by summing the mixture energy equation

$$\partial_t(\rho e) + \boldsymbol{\nabla}\cdot(\rho e\boldsymbol{u}) + p\,\boldsymbol{\nabla}\cdot\boldsymbol{u} = 0, \tag{A1}$$

the radiation energy equation

$$\partial_t E_r + \boldsymbol{\nabla}\cdot(E_r\boldsymbol{u}) + p_r\boldsymbol{\nabla}\cdot\boldsymbol{u} = 0, \tag{A2}$$

and the dot product of the momentum equation (4.1*d*) with the velocity vector. Specifically, performing a dot product on both sides of (4.1*d*) with $\boldsymbol{u}$ gives

$$\boldsymbol{u}\cdot[\partial_t(\rho\boldsymbol{u}) + \boldsymbol{\nabla}\cdot(\rho\boldsymbol{u}\boldsymbol{u})] + \boldsymbol{u}\cdot\boldsymbol{\nabla}p_t = \sigma\kappa\,\boldsymbol{\nabla}\phi\cdot\boldsymbol{u}, \tag{A3}$$

and by applying the identity

$$\begin{cases} \boldsymbol{u}\cdot\partial_t(\rho\boldsymbol{u}) = \partial_t\left(\rho|\boldsymbol{u}|^2/2\right), \\ \boldsymbol{u}\cdot\boldsymbol{\nabla}\cdot(\rho\boldsymbol{u}\boldsymbol{u}) = \boldsymbol{\nabla}\cdot\left(\rho|\boldsymbol{u}|^2\boldsymbol{u}/2\right), \\ \boldsymbol{u}\cdot\boldsymbol{\nabla}p_t = \boldsymbol{\nabla}\cdot\left(p_t\boldsymbol{u}\right) - p_t\boldsymbol{\nabla}\cdot\boldsymbol{u}, \end{cases} \tag{A4}$$

we can obtain

$$\partial_t\left(\rho|\boldsymbol{u}|^2/2\right) + \boldsymbol{\nabla}\cdot\left(\rho|\boldsymbol{u}|^2\boldsymbol{u}/2\right) + \boldsymbol{\nabla}\cdot\left(p_t\boldsymbol{u}\right) - p_t\boldsymbol{\nabla}\cdot\boldsymbol{u} = \sigma\kappa\,\boldsymbol{\nabla}\phi\cdot\boldsymbol{u}. \tag{A5}$$

Thus the sum of (A1), (A2) and (A5) leads to the convection equation of the total energy density as

$$\partial_t\,(\rho e_t) + \boldsymbol{\nabla}\cdot(\rho e_t\boldsymbol{u}) + \boldsymbol{\nabla}\cdot(p_t\boldsymbol{u}) = \sigma\kappa\,\boldsymbol{\nabla}\phi\cdot\boldsymbol{u}. \tag{A6}$$

Appendix B. Jacobian matrix and eigenvalues for the hyperbolic system

The hyperbolic subsystem (4.1*a*)–(4.1*d*), (A1) and (A2), in one-dimensional cases, can be rewritten in terms of the conservative variables $\boldsymbol{U} = (\rho_l\alpha_l,\ \rho_g\alpha_g,\ \rho u,\ \rho e,\ E_r,\ \alpha_l)^{\mathrm{T}}$ as

$$\partial_t\boldsymbol{U} + \boldsymbol{A}(\boldsymbol{U})\,\partial_x\boldsymbol{U} = 0. \tag{B1}$$

The Jacobian matrix $\boldsymbol{A}$ is written in the form

$$\boldsymbol{A} = \begin{bmatrix} \dfrac{\rho_g\alpha_g u}{\rho} & -\dfrac{\rho_l\alpha_l u}{\rho} & \dfrac{\rho_l\alpha_l}{\rho} & 0 & 0 & 0 \\ -\dfrac{\rho_g\alpha_g u}{\rho} & \dfrac{\rho_l\alpha_l u}{\rho} & \dfrac{\rho_g\alpha_g}{\rho} & 0 & 0 & 0 \\ -u^2 & -u^2 & 2u & \gamma-1 & \dfrac{1}{3} & W \\ -\dfrac{(\rho e+p)u}{\rho} & -\dfrac{(\rho e+p)u}{\rho} & \dfrac{\rho e+p}{\rho} & u & 0 & 0 \\ -\dfrac{(E_r+p_r)u}{\rho} & -\dfrac{(E_r+p_r)u}{\rho} & \dfrac{E_r+p_r}{\rho} & 0 & u & 0 \\ 0 & 0 & 0 & 0 & 0 & u \end{bmatrix}, \tag{B2}$$

https://doi.org/10.1017/jfm.2026.11808 Published online by Cambridge University Press

where $W = \partial p/\partial \alpha_l$. By applying the EOS of the mixture (3.7), it can be written as

$$W = \frac{(\gamma - 1)^2}{(\gamma_l - 1)\left(\gamma_g - 1\right)} \left(\left(\gamma_l - \gamma_g\right) \rho e + \gamma_g P_{\infty,g} - \gamma_l P_{\infty,l}\right). \tag{B3}$$

Matrix $\boldsymbol{A}$ possesses six real eigenvalues, i.e. $\{u, u, u, u, u - C_s, u + C_s\}$, where the characteristic wave speed C_s of the system is expressed as

$$C_s = \sqrt{C^2 + \frac{4p_r}{3\rho}}. \tag{B4}$$

Then the right eigenvectors of the matrix $\boldsymbol{A}$ are

$$\begin{aligned}
&\boldsymbol{R}_1(\boldsymbol{U}) = (0, 0, 0, -W, 0, \gamma - 1)^{\mathrm{T}},\\
&\boldsymbol{R}_2(\boldsymbol{U}) = (0,\ 0,\ 0,\ -1,\ 3(\gamma - 1),\ 0)^{\mathrm{T}},\\
&\boldsymbol{R}_3(\boldsymbol{U}) = (1,\ 0,\ u,\ 0,\ 0,\ 0)^{\mathrm{T}},\\
&\boldsymbol{R}_4(\boldsymbol{U}) = (-1,\ 1,\ 0,\ 0,\ 0,\ 0)^{\mathrm{T}},\\
&\boldsymbol{R}_5(\boldsymbol{U}) = (\rho_l\alpha_l,\ \rho_g\alpha_g,\ \rho(u - C_s),\ \rho C^2/(\gamma - 1),\ 4p_r,\ 0)^{\mathrm{T}},\\
&\boldsymbol{R}_6(\boldsymbol{U}) = (\rho_l\alpha_l,\ \rho_g\alpha_g,\ \rho(u + C_s),\ \rho C^2/(\gamma - 1),\ 4p_r,\ 0)^{\mathrm{T}}.
\end{aligned} \tag{B5}$$

Appendix C. Calculation of the mixture internal energy and radiation energy from the total energy

Advancing (4.1) from the n time step to the intermediate state $(*)$ would yield the total energy $(\rho e_t)^*$. However, our target variables are the internal energy $(\rho e)^*$ and the radiation energy $(E_r)^*$. The main reason why we do not directly advance (A1) and (A2) is that the calculation of the pressure work terms involving $\boldsymbol{\nabla \cdot u}$ becomes problematic in the presence of shocks.

The discretised form of (A1) and (A2) indicates the energy increments due to advection (superscript adv) and pressure work (superscript $work$):

$$(\rho e)^* - (\rho e)^n = \underbrace{-\boldsymbol{\nabla \cdot} (\rho e \boldsymbol{u})^n \Delta t}_{\Delta(\rho e)^{adv}} \ \underbrace{-(p \boldsymbol{\nabla \cdot u})^n \Delta t}_{\Delta(\rho e)^{work}}, \tag{C1}$$

$$(E_r)^* - (E_r)^n = \underbrace{-\boldsymbol{\nabla \cdot} (E_r \boldsymbol{u})^n \Delta t}_{\Delta(E_r)^{adv}} \ \underbrace{-(p_r \boldsymbol{\nabla \cdot u})^n \Delta t}_{\Delta(E_r)^{work}}. \tag{C2}$$

Energy conservation requires that

$$\Delta\left(\rho e_t\right) = \Delta\left(\rho e_k\right) + \Delta\left(\rho e\right)^{adv} + \Delta\left(E_r\right)^{adv} + \Delta\left(\rho e\right)^{work} + \Delta\left(E_r\right)^{work}, \tag{C3}$$

where the increments on the total energy $(\Delta(\rho e_t))$ and the kinetic energy $(\Delta(\rho e_k))$ have been computed via

$$\begin{cases} \Delta\left(\rho e_t\right) = (\rho e_t)^* - (\rho e_t)^n, \\ \Delta\left(\rho e_k\right) = \left(\rho\left|\boldsymbol{u}\right|^2/2\right)^* - \left(\rho\left|\boldsymbol{u}\right|^2/2\right)^n. \end{cases} \tag{C4}$$

We then need to find the four unknowns $\Delta(\rho e)^{adv}$, $\Delta(E_r)^{adv}$, $\Delta(\rho e)^{work}$, $\Delta(E_r)^{work}$.

The energy advections, i.e. $\Delta(\rho e)^{adv}$ and $\Delta(E_r)^{adv}$, are computed by being concurrently advanced with the hyperbolic subsystem (4.1). Then the pressure works

https://doi.org/10.1017/jfm.2026.11808 Published online by Cambridge University Press

($\Delta(\rho e)^{work}$ and $\Delta(E_r)^{work}$) are determined by applying the ratio p_r/p from (C1) and (C2):

$$\begin{cases} \Delta(\rho e)^{work} = \dfrac{p}{p+p_r}\left(\Delta(\rho e_t) - \Delta(\rho e_k) - \Delta(\rho e)^{adv} - \Delta(E_r)^{adv}\right), \\ \Delta(E_r)^{work} = \dfrac{p_r}{p+p_r}\left(\Delta(\rho e_t) - \Delta(\rho e_k) - \Delta(\rho e)^{adv} - \Delta(E_r)^{adv}\right). \end{cases} \tag{C5}$$

Finally, $(\rho e)^*$ and $(E_r)^*$ can be calculated by (C1) and (C2).

Appendix D. Formulae for the physical models employed in the simulation of laser–droplet interaction

In this paper, a series of physical models is used for simulating the pre-pulse scenario in LPP-EUV. In particular, the ionisation degree (Z_g) is modelled by the Thomas–Fermi theory (More 1985), the thermal conduction coefficient (λ_g) is modelled by the Spitzer–Härm theory (Spitzer & Härm 1953), and the radiative transport coefficients ($\chi_{r,g}$, $\omega_{r,g}$) are modelled by the empirical formulae from Tsakiris & Eidmann (1987).

D.1. *Thomas–Fermi model*

The Thomas–Fermi model (More 1985) provides a useful approximation for the ionisation degree Z_g in high-density plasmas (e.g. LPP in EUV), specifically as

$$Z_g = \frac{x}{1+x+\sqrt{1+2x}}Z, \tag{D1}$$

in which

$$\begin{cases} x = \eta\left(\dfrac{\rho_g}{AZ}\right)^{\zeta}\left[1+\left(a_1\left(\dfrac{T_g}{Z^{4/3}}\right)^{a_2} + a_3\left(\dfrac{T_g}{Z^{4/3}}\right)^{a_4}\right)^{L}\left(\dfrac{\rho_g}{AZ}\right)^{(N-1)L}\right]^{\beta/L}, \\ N = -\exp\left(b_0 + b_1\left(\dfrac{T_g}{Z^{4/3}+T_g}\right) + b_2\left(\dfrac{T_g}{Z^{4/3}+T_g}\right)^2\right), \\ L = c_1\dfrac{T_g}{Z^{4/3}+T_g} + c_2, \end{cases} \tag{D2}$$

where the coefficients are $\eta = 14.3139$, $\zeta = 0.6624$, $a_1 = 0.003323$, $a_2 = 0.9718$, $a_3 = 9.26148 \times 10^{-5}$, $a_4 = 3.10165$, $b_0 = -1.763$, $b_1 = 1.43175$, $b_2 = 0.31546$, $c_1 = -0.366667$ and $c_2 = 0.983333$. Here, ρ_g and T_g are the density and temperature of the plasma, in units g cm^{-3} and eV, respectively, and A and Z are the mass and atomic number of the element, respectively. Specifically, $A = 118$ and $Z = 50$ for tin.

D.2. *Spitzer–Härm theory*

The Spitzer–Härm theory (Spitzer & Härm 1953) captures the dominant collisional energy exchange in high-temperature plasmas, ensuring local thermodynamic equilibrium. These

https://doi.org/10.1017/jfm.2026.11808 Published online by Cambridge University Press

conditions are approximately satisfied in the bulk region of our simulation domain:

$$\lambda_g = \left(\frac{8}{\pi}\right)^{3/2} \frac{k_B^{7/2}}{e^4\sqrt{m_e}} \left(\frac{1}{1+3.3/Z_g}\right) \frac{T_g^{5/2}}{Z_g \ln \Lambda}, \tag{D3}$$

where $k_B = 1.3807 \times 10^{-16}$ g cm^2 s^{-2} K^{-1} is the Boltzmann constant, $e = 4.8032 \times 10^{-10}$ statcoulomb is the electron charge, and $m_e = 9.1094 \times 10^{-28}$ g is the mass of an electron. Also, $\ln \Lambda$ is the Coulomb logarithm given by

$$\ln \Lambda = \ln \left[\sqrt{\frac{k_B T_g}{4\pi e^2 n_e}} \Big/ \max\left(\frac{Z_g e^2}{3k_B T_g}, \frac{\hbar}{2\sqrt{3k_B T_g m_e}} \right) \right], \tag{D4}$$

where $n_e = \rho_g Z_g N_A / M_g$ is the electron number density (unit cm^{-3}, with $N_A = 6.022 \times 10^{23}$ mol^{-1} the Avogadro constant) and $\hbar = 1.0546 \times 10^{-27}$ g cm^2 s^{-1} is the reduced Planck constant.

D.3. *Radiation empirical formulae*

The radiative transport coefficients ($\chi_{r,g}$, $\omega_{r,g}$) can be written in the form

$$\begin{cases} \chi_{r,g} = \dfrac{ac}{3\rho_g \sigma_R}, \\ \omega_{r,g} = ac\rho_g \sigma_P, \end{cases} \tag{D5}$$

where a is the radiation constant, and $c = 3 \times 10^{10}$ cm s^{-1} is the speed of light in vacuum. The Rossland σ_R and Planck σ_P mean opacities are given by the empirical formulae taken from Tsakiris & Eidmann (1987), which have been proven to be useful in the study of phenomena in hydrodynamics involving radiative energy transport (e.g. high-temperature high-density plasma):

$$\begin{cases} \sigma_R \text{ [cm}^2 \text{ g}^{-1}\text{]} = 72.19 T_g^{-1.571} \text{ [keV]} \ \rho_g^{0.16} \text{ [g cm}^{-3}\text{]}, \\ \sigma_P \text{ [cm}^2 \text{ g}^{-1}\text{]} = 328.55 T_g^{-1.588} \text{ [keV]} \ \rho_g^{0.228} \text{ [g cm}^{-3}\text{]}. \end{cases} \tag{D6}$$

References

Allaire, G., Clerc, S. & Kokh, S. 2002 A five-equation model for the simulation of interfaces between compressible fluids. *J. Comput. Phys.* **181**, 577–616.

Basko, M.M., Novikov, V.G. & Grushin, A.S. 2015 On the structure of quasi-stationary laser ablation fronts in strongly radiating plasmas. *Phys. Plasmas* **22**, 053111.

Basko, M.M., Sasorov, P.V., Murakami, M., Novikov, V.G. & Grushin, A.S. 2012 One-dimensional study of the radiation-dominated implosion of a cylindrical tungsten plasma column. *Plasma Phys. Control. Fusion* **54**, 055003.

Bo, W. & Grove, J.W. 2014 A volume of fluid method based ghost fluid method for compressible multi-fluid flows. *Comput. Fluids* **90**, 113–122.

Castor, J.I. 2004 *Radiation Hydrodynamics*. Cambridge University Press.

Faik, S., Basko, M.M., Tauschwitz, A., Iosilevskiy, I. & Maruhn, J.A. 2012 Dynamics of volumetrically heated matter passing through the liquid–vapor metastable states. *High Energy Density Phys.* **8**, 349–359.

França, H.L., Schubert, H.K., Versolato, O. & Jalaal, M. 2025 Laser-induced droplet deformation: curvature inversion explained from instantaneous pressure impulse. *J. Fluid Mech.* **1020**, A21.

Fryxell, B., Olson, K., Ricker, P., Timmes, F.X., Zingale, M., Lamb, D.Q., MacNeice, P., Rosner, R., Truran, J.W. & Tufo, H. 2000 FLASH: an adaptive mesh hydrodynamics code for modeling astrophysical thermonuclear flashes. *Astrophys. J. Suppl. Ser.* **131**, 273.

https://doi.org/10.1017/jfm.2026.11808 Published online by Cambridge University Press

FYFE, D.E., ORAN, E.S. & FRITTS, M.J. 1988 Surface tension and viscosity with Lagrangian hydrodynamics on a triangular mesh. *J. Comput. Phys.* **76**, 349–384.

GARRICK, D.P., OWKES, M. & REGELE, J.D. 2017 A finite-volume HLLC-based scheme for compressible interfacial flows with surface tension. *J. Comput. Phys.* **339**, 46–67.

GELDERBLOM, H., LHUISSIER, H., KLEIN, A.L., BOUWHUIS, W., LOHSE, D., VILLERMAUX, E. & SNOEIJER, J.H. 2016 Drop deformation by laser-pulse impact. *J. Fluid Mech.* **794**, 676–699.

HAWKER, N.A. & VENTIKOS, Y. 2012 Interaction of a strong shockwave with a gas bubble in a liquid medium: a numerical study. *J. Fluid Mech.* **701**, 59–97.

HERNANDEZ-RUEDA, J., LIU, B., HEMMINGA, D.J., MOSTAFA, Y., MEIJER, R.A., KURILOVICH, D., BASKO, M., GELDERBLOM, H., SHEIL, J. & VERSOLATO, O.O. 2022 Early-time hydrodynamic response of a tin droplet driven by laser-produced plasma. *Phys. Rev. Res.* **4**, 013142.

JOHNSEN, E. & COLONIUS, T. 2006 Implementation of WENO schemes in compressible multicomponent flow problems. *J. Comput. Phys.* **219** (2), 715–732.

KAPILA, A.K., MENIKOFF, R., BDZIL, J.B., SON, S.F. & STEWART, D.S. 2001 Two-phase modeling of deflagration-to-detonation transition in granular materials: reduced equations. *Phys. Fluids* **13**, 3002–3024.

VAN DE KERKHOF, M. *et al.* 2020 Spectral purity performance of high-power EUV systems. In *Extreme Ultraviolet (EUV) Lithography XI* (ed. N.M. Felix & A. Lio), vol. 11323, p. 1132321. International Society for Optics and Photonics, SPIE.

KHARBEDIA, M., LIU, B., MEIJER, R., ENGELS, D.J., SCHUBERT, K., BOUROUIBA, L. & VERSOLATO, O. 2026 Rim destabilisation and re-formation upon severance from its fragmenting expanding sheet. *J. Fluid Mech.* **1030**, A57.

KLEIN, A.L., BOUWHUIS, W., VISSER, C.W., LHUISSIER, H., SUN, C., SNOEIJER, J.H., VILLERMAUX, E., LOHSE, D. & GELDERBLOM, H. 2015 Drop shaping by laser-pulse impact. *Phys. Rev. Appl.* **3**, 044018.

KLEIN, A.L., KURILOVICH, D., LHUISSIER, H., VERSOLATO, O.O., LOHSE, D., VILLERMAUX, E. & GELDERBLOM, H. 2020 Drop fragmentation by laser-pulse impact. *J. Fluid Mech.* **893**, A7.

KRALL, N.A. & TRIVELPIECE, A.W. 1973 *Principles of Plasma Physics*. McGraw-Hill.

KRUER, W.L. 1988 *The Physics of Laser Plasma Interactions*. Addison-Wesley Publishing Co.

KURILOVICH, D., BASKO, M.M., KIM, D.A., TORRETTI, F., SCHUPP, R., VISSCHERS, J.C., SCHEERS, J., HOEKSTRA, R., UBACHS, W. & VERSOLATO, O.O. 2018 Power-law scaling of plasma pressure on laser-ablated tin microdroplets. *Phys. Plasmas* **25**, 012709.

KURILOVICH, D., KLEIN, A.L., TORRETTI, F., LASSISE, A., HOEKSTRA, R., UBACHS, W., GELDERBLOM, H. & VERSOLATO, O.O. 2016 Plasma propulsion of a metallic microdroplet and its deformation upon laser impact. *Phys. Rev. Appl.* **6**, 014018.

LE MÉTAYER, O., MASSONI, J. & SAUREL, R. 2004 Élaboration des lois d'état d'un liquide et de sa vapeur pour les modèles d'écoulements diphasiques. *Intl J. Therm. Sci.* **43**, 265–276.

LIN, J.Y., DING, H., LU, X.Y. & WANG, P. 2017 A comparison study of numerical methods for compressible two-phase flows. *Adv. Appl. Maths Mech.* **9**, 1111–1132.

LIU, B., HERNANDEZ-RUEDA, J., GELDERBLOM, H. & VERSOLATO, O.O. 2022 Speed of fragments ejected by an expanding liquid tin sheet. *Phys. Rev. Fluids* **7**, 083601.

LIU, W., KONIGES, A., GOTT, K., EDER, D., BARNARD, J., FRIEDMAN, A., MASTERS, N. & FISHER, A. 2017 Surface tension models for a multi-material ALE code with AMR. *Comput. Fluids* **151**, 91–101.

LONG, T., CAI, J. & PAN, S. 2023 A fully conservative sharp-interface method for compressible multiphase flows with phase change. *J. Comput. Phys.* **493**, 112501.

LOWRIE, R.B. & EDWARDS, J.D. 2008 Radiative shock solutions with grey nonequilibrium diffusion. *Shock Waves* **18**, 129–143.

MACFARLANE, J.J., GOLOVKIN, I.E. & WOODRUFF, P.R. 2006 HELIOS-CR-A 1-D radiation-magnetohydrodynamics code with inline atomic kinetics modeling. *J. Quant. Spectrosc. Radiat. Transfer* **99**, 381–397.

MCLACHLAN, R.I. & QUISPEL, G.R.W. 2002 Splitting methods. *Acta Numerica* **11**, 341–434.

MEIJER, R.A., KURILOVICH, D., EIKEMA, K.S.E., VERSOLATO, O.O. & WITTE, S. 2022 The transition from short- to long-timescale pre-pulses: laser-pulse impact on tin microdroplets. *J. Appl. Phys.* **131**, 105905.

MIN, Q. *et al.* 2024 RHDLPP: a multigroup radiation hydrodynamics code for laser-produced plasmas. *Comput. Phys. Commun.* **302**, 109242.

MIZOGUCHI, H. *et al.* 2010 First generation laser-produced plasma source system for HVM EUV lithography. In *Extreme Ultraviolet (EUV) Lithography* (ed. B.M. La Fontaine), vol. 7636, p. 763608. International Society for Optics and Photonics, SPIE.

MORE, R.M. 1985 Pressure ionization, resonances, and the continuity of bound and free states. *Adv. Atomic Mol. Phys.* **21**, 305–356.

https://doi.org/10.1017/jfm.2026.11808 Published online by Cambridge University Press

NISHIHARA, K. *et al.* 2008 Plasma physics and radiation hydrodynamics in developing an extreme ultraviolet light source for lithography. *Phys. Plasmas* **15**, 056708.

NOURGALIEV, R.R., DINH, T.N. & THEOFANOUS, T.G. 2006 Adaptive characteristics-based matching for compressible multifluid dynamics. *J. Comput. Phys.* **213**, 500–529.

NYKTERI, G. & GAVAISES, M. 2022 Numerical modeling of droplet rim fragmentation by laser-pulse impact using a multiscale two-fluid approach. *Phys. Rev. Fluids* **7**, 103604.

REIJERS, S.A., SNOEIJER, J.H. & GELDERBLOM, H. 2017 Droplet deformation by short laser-induced pressure pulses. *J. Fluid Mech.* **828**, 374–394.

REINICKE, P. & MEYER-TER-VEHN, J. 1991 The point explosion with heat conduction. *Phys. Fluids A* **3**, 1807–1818.

SHEIL, J., POIRIER, L., LASSISE, A.C., HEMMINGA, D.J., SCHOUWENAARS, S., BRAAKSMA, N., FRENZEL, A., HOEKSTRA, R. & VERSOLATO, O.O. 2024 Power-law scaling relating the average charge state and kinetic energy in expanding laser-driven plasmas. *Phys. Rev. Lett.* **133**, 125101.

SHEIL, J., VERSOLATO, O., BAKSHI, V. & SCOTT, H. 2023 Review of the 1st EUV light sources code comparison workshop. *Atoms* **11**, 130.

SHYUE, K. 1998 An efficient shock-capturing algorithm for compressible multicomponent problems. *J. Comput. Phys.* **142**, 208–242.

SIZYUK, T. & HASSANEIN, A. 2015 Extending the path for efficient extreme ultraviolet sources for advanced nanolithography. *Phys. Plasmas* **22**, 093101.

SPITZER, J.L. & HÄRM, R. 1953 Transport phenomena in a completely ionized gas. *Phys. Rev.* **89**, 977.

TAO, T. *et al.* 2025 A rasterization-based ray-tracing method for laser-plasma interactions. *High Power Laser Sci. Engng* **13**, e37.

TORO, E.F. 2013 *Riemann Solvers and Numerical Methods for Fluid Dynamics: A Practical Introduction*. Springer Science & Business Media.

TSAKIRIS, G.D. & EIDMANN, K. 1987 An approximate method for calculating Planck and Rosseland mean opacities in hot, dense plasmas. *J. Quant. Spectrosc. Radiat. Transfer* **38**, 353–368.

VERSOLATO, O.O. 2019 Physics of laser-driven tin plasma sources of EUV radiation for nanolithography. *Plasma Sources Sci. Technol.* **28**, 083001.

VERSOLATO, O.O., SHEIL, J., WITTE, S., UBACHS, W. & HOEKSTRA, R. 2022 Microdroplet-tin plasma sources of EUV radiation driven by solid-state-lasers (topical review). *J. Opt.* **24**, 054014.

YUAN, Y., MA, Y.Y., WANG, W.P., CHEN, S.J., CUI, Y., ZI, M., YANG, X.H., ZHANG, G.B. & LENG, Y.X. 2022 Enhancing the conversion efficiency of extreme ultraviolet light sources using a 2 μm wavelength laser. *Plasma Phys. Control. Fusion* **64**, 025001.

https://doi.org/10.1017/jfm.2026.11808 Published online by Cambridge University Press